Research Square

Preprints are preliminary reports that have not undergone peer review.
They should not be considered conclusive, used to inform clinical practice,
or referenced by the media as validated information.

Analytical and Numerical Investigation of Frequency-Independent Tuned Inerter Outrigger Systems for Seismic and Wind Vibration Control of Tall Buildings

K. K. Kiran
SJB Institute of Technology
Naveenkumar D. T.
naveenkumardt@sjbit.edu.in

SJB Institute of Technology

Research Article

Keywords: Frequency-independent damping, Tuned inerter damper outrigger, Negative stiffness, Multimodal vibration control, Seismic and wind excitation, Tall buildings

Posted Date: November 5th, 2026

DOI: https://doi.org/10.21203/rs.3.rs-10493251/v1

License: This work is licensed under a Creative Commons Attribution 4.0 International License.
Read Full License

Additional Declarations: No competing interests reported.

Analytical and Numerical Investigation of Frequency-Independent Tuned Inerter Outrigger Systems for Seismic and Wind Vibration Control of Tall Buildings

K. K. Kiran[1] and Naveenkumar D. T.[2*]

[1,2] Department of Civil Engineering, SJB Institute of Technology, Bangalore, Karnataka, India
*Corresponding Author: naveendt012@gmail.com
Orcid: 0000-0001-8512-2442

Abstract

The increasing construction of tall and slender buildings has intensified the need for passive vibration control systems for mitigating structural responses under seismic and wind excitations. Conventional damped outrigger systems are generally tuned to dominant vibration modes and exhibit reduced effectiveness under broadband dynamic excitations involving significant higher-mode participation. This study presents a comprehensive analytical framework for two frequency-independent passive outrigger systems, namely the Frequency-Independent Tuned Inerter Damper Outrigger (FI-TIDO) and the Frequency-Independent Negative Stiffness Damper Outrigger (FI-NSDO), for multimodal vibration control of tall buildings. Closed-form analytical formulations are developed to characterize the equivalent dynamic behaviour of the proposed systems, while a numerical optimization procedure determines their optimal design parameters. By integrating frequency-independent hysteretic damping with inerter and negative stiffness mechanisms, the proposed configurations provide broadband vibration mitigation without tuning to a single structural frequency. Their performance is evaluated on a benchmark 60-story building subjected to seismic and crosswind excitations using frequency-domain and nonlinear time-history analyses. Results show that the proposed frequency-independent outrigger systems substantially enhance modal damping and vibration mitigation over a broad frequency range. The FI-TIDO system achieves a maximum first-mode damping ratio of 24.32%, compared with 2.89% for a conventional damped outrigger system, and reduces the average inter-story drift and floor acceleration by 32.5% and 23.45%, respectively, under eleven near-fault earthquake records. The developed analytical framework provides an efficient tool for the analysis, preliminary design, and optimization of advanced frequency-independent outrigger systems for tall buildings subjected to broadband seismic and wind excitations.

Keywords: Frequency-independent damping; Tuned inerter damper outrigger; Negative stiffness; Multimodal vibration control; Seismic and wind excitation; Tall buildings.

Statements and Declarations

Funding: The authors did not receive support from any organization for the submitted work.

Conflicts of interest/Competing interests: The authors have read the Committee on Publication Ethics guidelines and agree to abide by provisions thereof.

Availability of data and material: All the required data were generated by the authors using a software code written in MATLAB 7.0.

Authors' contributions: Both the authors have contributed to the study conception and design. Material preparation, data collection and analysis were performed by all theree authors. The first draft of the manuscript was written by Dr. Kiran K. K. and final revisions were made by Dr. Naveenkumar D. T. Both authors read and approved the final manuscript.

NOMENCLATURE

Abbreviations

CDO	Conventional Damped Outrigger
FID	Frequency-Independent-Damper
FI-NSDO	Frequency-Independent Negative Stiffness Damped Outrigger
FI-TIDO	Frequency-Independent Tuned Inerter Damped Outrigger
NSD	Negative Stiffness Damper
NSD-TID	Negative Stiffness Damper Tuned Inerter Damper
NSDO	Negative Stiffness Damped Outrigger
TID	Tuned Inerter Damper
TIDO	Tuned Inerter Damped Outrigger
TMD	Tuned Mass Damper
TMDI	Tuned Mass Damper Inerter
VD	Viscous Damper

Symbols

α	Position of the outrigger in tall structure
β	Outrigger stiffness
C	Damping matrix
c	Normalized outrigger damping
C_d	Damping coefficient
δ	Earthquake excitation
f_{NS}	Negative stiffness
F_d	Force at outrigger ends
F_{NSD}	Force exerted by NSD
FP_{FID}	Dynamic behaviour of FID
F_{VD}	Dynamic force of linear viscous damper
$H[\bullet]$	Hilbert transform
K	Stiffness matrix
k_c	Equivalent stiffness of outrigger
K_d	Damper stiffness
k_{NS}	Negative stiffness
K_s	Stiffness of the spring
k_s	Equivalent stiffness of NSDO
$k\theta$	Rotational resistant stiffness
L_1, L_2, L_s & L_p	Lengths depicted
M	Mass matrix
$M\theta$	Resisting moment provided outrigger damped
μ	Inertance ratio
η	Negative stiffness ratio
ω	Loading frequency
ω_f	Frequency of filter materials
ω_g	Frequency of soil materials

$\bar{\omega}$	Frequency of outrigger system
φ	Frequency-independent loss modulus
ϕ	Loss factor
P_{in}	Pre compression of the spring
P_S	Output variable vector
ψ	Position vector of outrigger
r	Outrigger length
$S=i\omega$	Laplace variable
S_o	Intensity of white noise process
$S_{EQ}(\omega)$	PSD matrix of earthquake excitation
$S\ddot{Y}(\omega)$	Seismic acceleration response
$S_Y(\omega)$	Seismic displacement response
T	Transpose
U(z)	Wind velocity profile
U	Deformation of Laplace-domain
u	Damper deformation
u_c	Deformation of outrigger
$\ddot{x}_g$	Ground excitation
ξ	Modal damping ratio
ξ_f	Damping ratio of filter materials
ξ_g	Damping ratio of soil materials
k_d	Damper stiffness
λ^4	Normalized frequency
y	Displacement vector including transverse displacement and rotational deformation

1.0 INTRODUCTION

The rapid pace of urbanization and increasing scarcity of available land have accelerated the construction of tall and slender buildings worldwide. While these structures offer efficient utilization of urban space, their increasing height and flexibility make them highly susceptible to dynamic actions such as earthquakes and strong winds. Because modern tall buildings typically possess low inherent damping ratios, often less than 1%, excessive lateral displacements, inter-story drifts, floor accelerations, and occupant discomfort may occur under moderate to severe dynamic excitations (Smith et al. 2010; Zhou et al. 2022; Gu et al. 2022). Among these hazards, crosswind excitation is particularly critical because vortex shedding frequencies may coincide with the natural frequencies of slender buildings, producing resonance and significant amplification of structural responses (Kawai 1992; Lamb and Kwok 2017). Consequently, ensuring adequate structural safety, serviceability, and occupant comfort under both seismic and wind loading has become one of the principal challenges in the design of modern high-rise buildings.

To enhance the lateral stiffness and dynamic performance of tall buildings, outrigger systems have become one of the most widely adopted structural control strategies. By coupling the central core to the perimeter columns, outriggers effectively reduce overturning moments, lateral displacements, and inter-story drifts while improving the overall structural efficiency. In recent years, conventional outrigger systems have evolved into virtual and hybrid configurations to achieve improved structural performance together with greater architectural flexibility. Parametric investigations have shown that the effectiveness of outrigger systems depends strongly on structural height, stiffness distribution, and outrigger location under both seismic and wind loading (John and Kamath 2023). Recent studies

have also demonstrated that optimized hybrid outrigger systems can significantly improve the seismic and wind resistance of tall buildings through appropriate selection of outrigger configuration and location.

In addition to outrigger systems, numerous passive vibration control devices have been developed to improve the seismic and wind performance of high-rise structures. Tuned Mass Dampers (TMDs), Tuned Liquid Dampers (TLDs), Conventionally Damped Outriggers (CDOs), viscous dampers, and Tuned Mass Damper Inerters (TMDIs) have been extensively employed to reduce structural responses through supplemental energy dissipation (Aly 2014; Daniel and Lavan 2014; Kaveh et al. 2015; Elias and Matsagar 2018; Kamgar et al. 2020; Kaveh et al. 2020; Wang et al. 2024). Recent investigations have further demonstrated the effectiveness of tuned mass dampers in regular and irregular high-rise buildings considering soil–structure interaction, highlighting the importance of optimized damper placement for enhancing seismic resilience (Kamgar et al. 2020; Kontoni and Farghaly 2023; Kontoni and Farghaly 2024a; Kontoni and Farghaly 2024b). Furthermore, optimization-based vibration control strategies and novel tuned mass damper configurations have demonstrated significant improvements in mitigating seismic responses of civil engineering structures (Khatibinia et al. 2025; Kiran et al. 2025; Kiran and Naveenkumar 2025a; Li et al. 2026). Despite these advances, conventional TMDs remain inherently frequency-dependent and are generally effective only within a narrow frequency band centred around their tuning frequency. Similarly, conventionally damped outrigger systems primarily suppress the dominant structural mode, and their effectiveness diminishes as higher-mode participation becomes significant (Vickery et al. 1983; Banavalkar 1990). Consequently, these systems may not provide satisfactory vibration mitigation under broadband seismic and crosswind excitations where multiple structural modes contribute simultaneously to the overall response.

To overcome these limitations, researchers have developed several enhanced passive control systems incorporating viscous dampers, Maxwell damping elements, metallic yielding dampers, magnetorheological dampers, shape memory alloys, inerters, and negative stiffness mechanisms (Constantinou et al. 2001; Asai et al. 2013; Lin et al. 2018; Liu et al. 2018; Das and Tesfamariam 2020; Wang et al. 2020; Dai et al. 2022; Nagarajaiah et al. 2022; Wang et al. 2026). Among these developments, Tuned Inerter Damper Outriggers (TIDOs) have attracted considerable attention because the inerter substantially amplifies the apparent inertia without introducing excessive additional mass, thereby improving vibration suppression efficiency (Aly 2014; Wang et al. 2020). Similarly, Negative Stiffness Devices (NSDs) have been successfully integrated into structural control systems to increase equivalent damping while avoiding excessive increases in structural stiffness (Sun et al. 2017; Cimellaro et al. 2020; Wang et al. 2022a; Kiran et al. 2022; Kiran et al. 2023). Recent analytical investigations have further demonstrated the advantages of inerter-assisted vibration control and nonlinear negative stiffness mechanisms for improving structural performance under harmonic and seismic excitations (Kiran and Naveenkumar 2024; Kiran and Naveenkumar 2025b; Chowdhury and Debbarma 2026; Kiran and Naveenkumar 2026). Despite these developments, the majority of these systems continue to rely on frequency-dependent tuning and therefore exhibit reduced effectiveness under broadband dynamic excitations such as near-fault earthquakes and crosswind loading, where multiple vibration modes contribute significantly to the structural response.

Recent studies have increasingly focused on combining inerters, negative stiffness mechanisms, and supplemental damping to achieve enhanced multimodal vibration mitigation in tall buildings (Wang et al. 2020; Wang et al. 2022a; Nagarajaiah et al. 2022; Wang et al. 2023; Huang and Zhu 2026). Although these hybrid systems demonstrate superior performance compared with conventional passive control devices, most investigations have considered either seismic or wind loading individually, while relatively few studies have examined their effectiveness under both broadband seismic and crosswind excitations. Moreover, recent analytical developments on nonlinear negative stiffness systems and inerter-assisted vibration isolation have demonstrated the advantages of integrating multiple passive control mechanisms; however, the application of frequency-independent damping concepts to outrigger systems remains largely unexplored (Kiran and Naveenkumar 2024; Kiran and Naveenkumar 2026). In particular, closed-form analytical formulations for evaluating the equivalent dynamic characteristics, rotational stiffness relationships, and multimodal vibration control capabilities of frequency-independent inerter-based outrigger systems have not yet been established. Such formulations are particularly valuable during the preliminary design stage of tall buildings, where rapid evaluation of passive vibration control systems is essential before detailed numerical simulations are undertaken. Motivated by these research gaps, the present study develops two frequency-independent outrigger systems, namely the Frequency-Independent Tuned Inerter Damper Outrigger (FI-TIDO) and the Frequency-Independent Negative Stiffness Damper Outrigger (FI-NSDO), and establishes a comprehensive analytical framework for evaluating their dynamic characteristics and vibration control performance under seismic and wind excitations.

The principal contributions of this study are summarized as follows:

1. An analytical framework is developed for designing frequency-independent tuned inerter outrigger systems for tall buildings using Laplace-domain and state-space formulations.
2. Closed-form equivalent rotational stiffness relationships are established to characterize the frequency-independent dynamic behaviour of the proposed outrigger systems.
3. The influence of damping ratio, stiffness ratio, inertance ratio, negative stiffness, and outrigger location on multimodal vibration mitigation is systematically investigated.
4. The seismic and crosswind performance of the proposed FI-TIDO and FI-NSDO systems is comprehensively evaluated using both frequency-domain and nonlinear time-history analyses.
5. Comparative performance assessments are conducted against existing damped outrigger systems and recently reported inerter-assisted configurations using a benchmark 60-story building.

The remainder of this paper is organized as follows. Section 2 presents the theoretical formulation of the proposed frequency-independent outrigger systems. Section 3 investigates their dynamic characteristics. Sections 4 and 5 evaluate the seismic and crosswind performance of the proposed systems, respectively. Section 6 presents comparative assessments with existing outrigger configurations, Section 7 provides numerical validation of the proposed analytical formulations, and Section 8 summarizes the major findings and conclusions.

2.0 FREQUENCY-INDEPENDENT OUTRIGGER WITH DIFFERENT DAMPER

2.1 Dynamic Characteristics of Frequency-Independent and Viscous Dampers

Typical linear viscous damping force is expressed as:

$$F_{VD} = k_d u + c_d \dot{u} \tag{1}$$

where k_d and c_d, are damper stiffness and coefficient respectively; u is damper deformations; and dot is represented as a derivative of time.

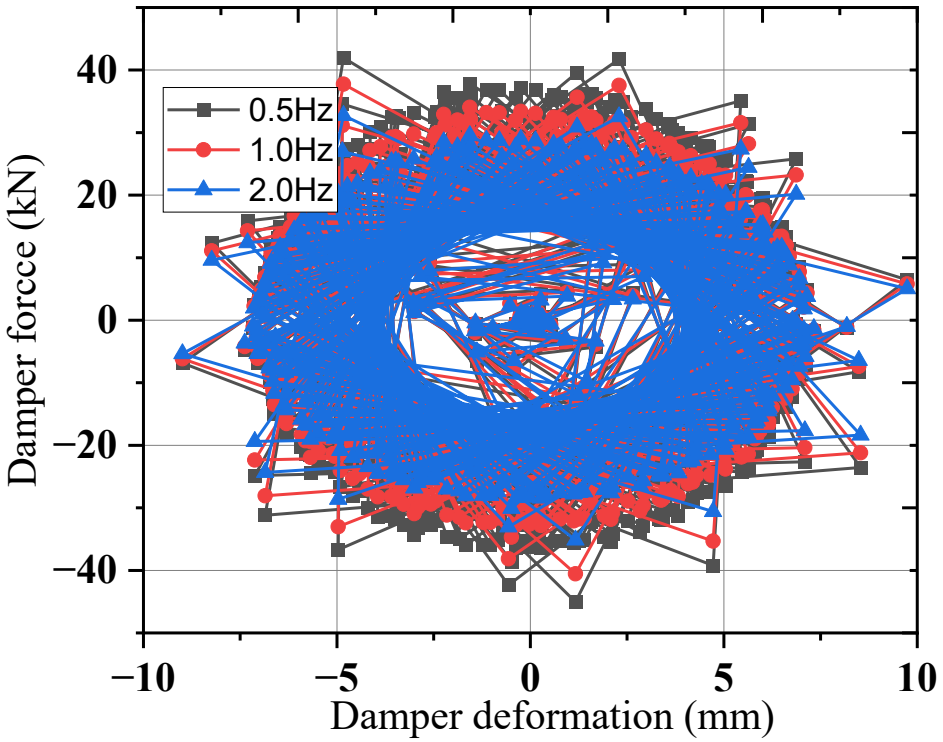
Laplace-domain yields are obtained from transforming of Eq. (1).

$$F_{VD} = k_d U + c_d U_s \tag{2}$$

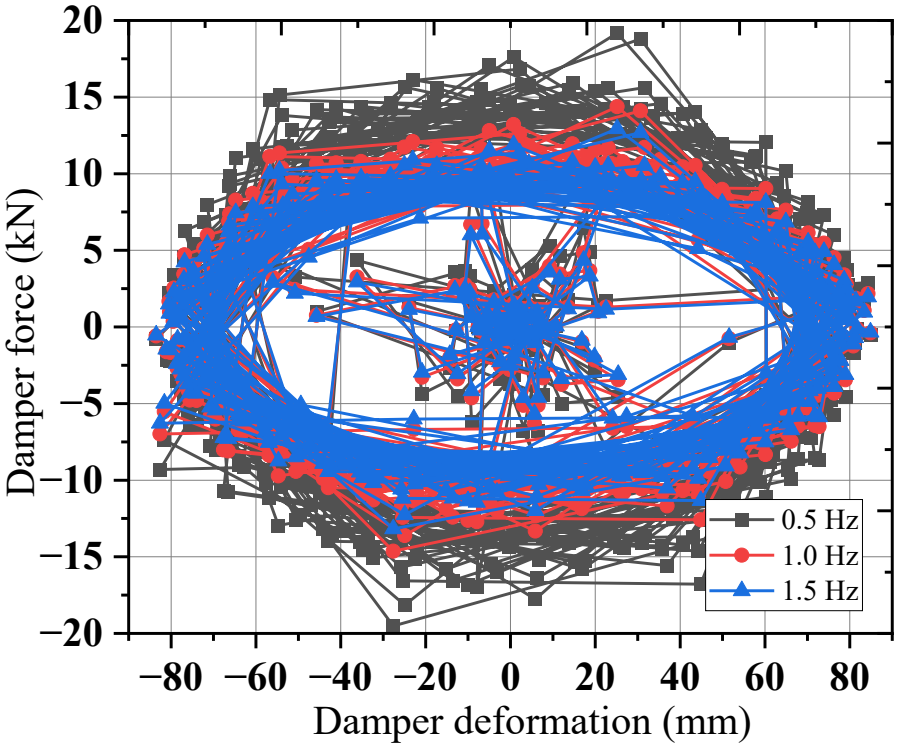
The loading frequency ω depends on the damping force, where $s = i\omega$ is the Laplace variable. U and U_s is deformation of the viscous damper and structural system respectively.

The force-deformation response of a viscous damper (VD) under sinusoidal loading at varying frequencies is shown in Fig. 1(a). As the frequencies increase, the corresponding damping force and energy dissipation increase. Nonetheless, different modes of vibrations consist of different frequencies, where the damping force increases with the increase in the mode. Therefore, multimodal vibration needs to compromise the efficiency of the optimal design of VD. The applications of VD find their way into different areas, including braced damper systems (Losanno et al. 2018; Wang et al. 2019), cable vibration (Javanbakht et al. 2020), and damped outrigger tall structures (Chen et al. 2010). Under sinusoidal excitations, the energy dissipation per cycle for a linear VD mode is directly proportional to the loading frequency, as demonstrated in Eq. (1) (Clough and Penzien 1975). The practical materials such as asphalt, acrylic polymers, and rubber investigated by the experimental method show minor dependence on frequency for energy dissipations (Markou and Manolis 2016). However, by using such materials, it is not possible to form a frequency-independent damper for energy dissipation as a sandwich type (Bae et al. 2014) and cables for high damping of rubber cables (Fujino and Hoang 2008). As described in the literature (Nagarajaiah and Sen 2020), the linear hysteric damper model for the dynamic behaviour of FID is represented as

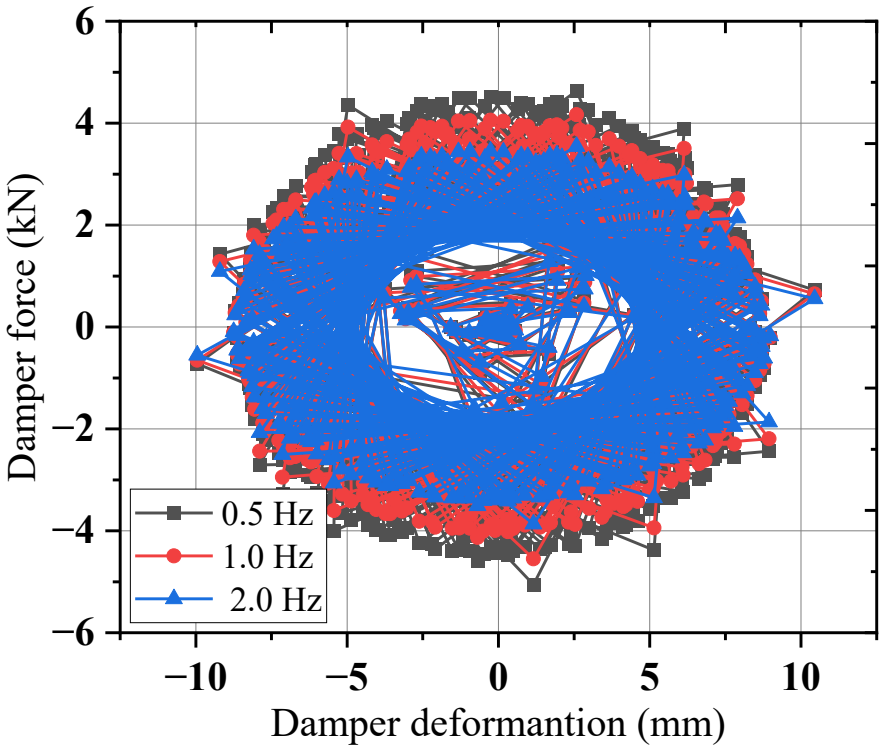
$$F_{FID} = (k_d + i\varphi)u = k_d(1 + i\phi)u \tag{3}$$


0.5Hz
1.0Hz
2.0Hz
Damper forcce (kN)
Damper deformation (mm)
40
20
0
−20
−40
−10
−5
0
5
10

(a) VD


0.5 Hz
1.0 Hz
1.5 Hz
Damper force (kN)
Damper deformation (mm)
20
15
10
5
0
−5
−10
−15
−20
−80
−60
−40
−20
0
20
40
60
80

(b) FID



(c) FITID

Fig. 1 Force–deformation responses under different loading frequencies: (a) VD; (b) FID; and (c) FITID.

where φ is frequency-independent loss modulus (the loss factor is a ratio of the loss and storage moduli) and i is the imaginary unit.

The displacement response is proportional to the FID's damping force, as observed in Eq. (3). The stiffness coefficient is also observed as a complex value, and frequency is an independent value. The FID is primarily designed for the first mode, and later it is of minimum importance to a higher-mode of vibrations, as shown in Fig. 1(b).

2.2 Comparisons of FID to its TID

The damping force of the model for a typical tuned inerter damper is represented as follows:

$$F_{TID} = k_d u^2 + c_d \dot{u} \tag{4}$$

where k_d and c_d, are the damper stiffness and coefficient, respectively, u is the damper deformations, and dot is represented as a derivative of time. Laplace-domain yields are obtained from transforming Eq. (4)

$$F_{TID} = k_d U^2 + c_d U_s \tag{5}$$

The loading frequency, ω, depends on the damping force, where $s = i\omega$ is the Laplace variable. It is found that damping force is directly proportional to damper deformation at different frequencies, as shown in Fig. 1(c).

2.3 Negative Stiffness Devices with Frequency-Independent Features

In this study, the NSD proposed by Nagarajaiah and Sen (Nagarajaiah and Sen 2020) is adopted for detuning the effect of existing tall structures by NSD-TID. The different components of NSD are a pivot plate, a pre-compressed spring,

hinged columns, chevrons, and others. The top and bottom chevrons are applied to relative deformations, resulting in the rotating spring and pivot plate. The controlled equations of NSD based on adaptative stiffness are expressed as:

$$F_{NSD} = -\left(\frac{P_{in} + K_S L_P}{L_S} - K_S\right)\left(\frac{L_1}{L_2}\right)\left(2 + \frac{L_2}{L_1} + \frac{L_P + L_1}{\sqrt{L_2^2 - q^2}}\right)u_d \quad (6)$$

For the detailed derivations of the above expressions, the study reported by Sarlis et al. (Sarlis et al. 2013) may be referred. For ideal NSD, Eq. (6) is simplified further as proportional to relative displacement, as expressed in Eq. (7):

$$f_{NS} = k_{NS} U \quad (7)$$

where force in the NSD is f_{NS}, relative deformations is U, and negative stiffness value is k_{NS}. It is observed from Eq. (7) that for different frequencies, the value attains a constant stiffness of NSD (k_{NS}) compared to the frequency-dependent values of viscous damper, mass, and inerter (Wang et al. 2022a; Nagarajaiah et al. 2022). Experimental tests were also conducted to prove that the NSD's behaviour is independent of the loading frequency based on dynamic characteristics (Wang et al. 2022a; Nagarajaiah et al. 2022). Fig. 2 shows the comparisons of analytical results and experimental measurements for the normalized loop of force and displacement.

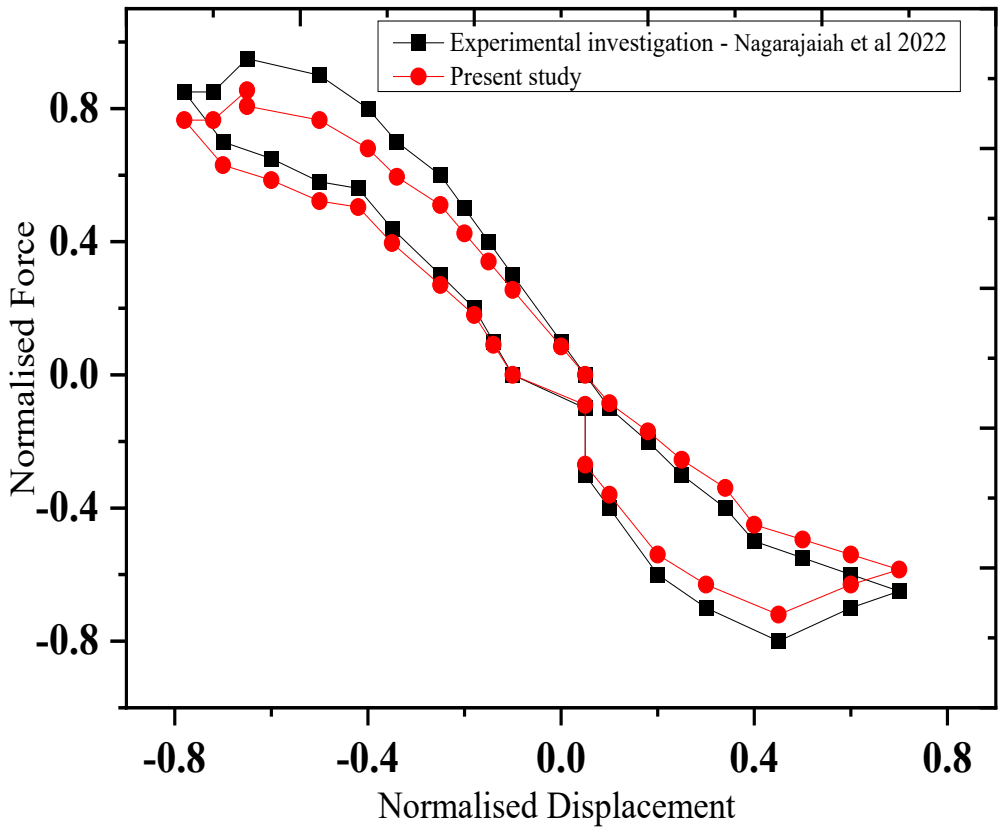


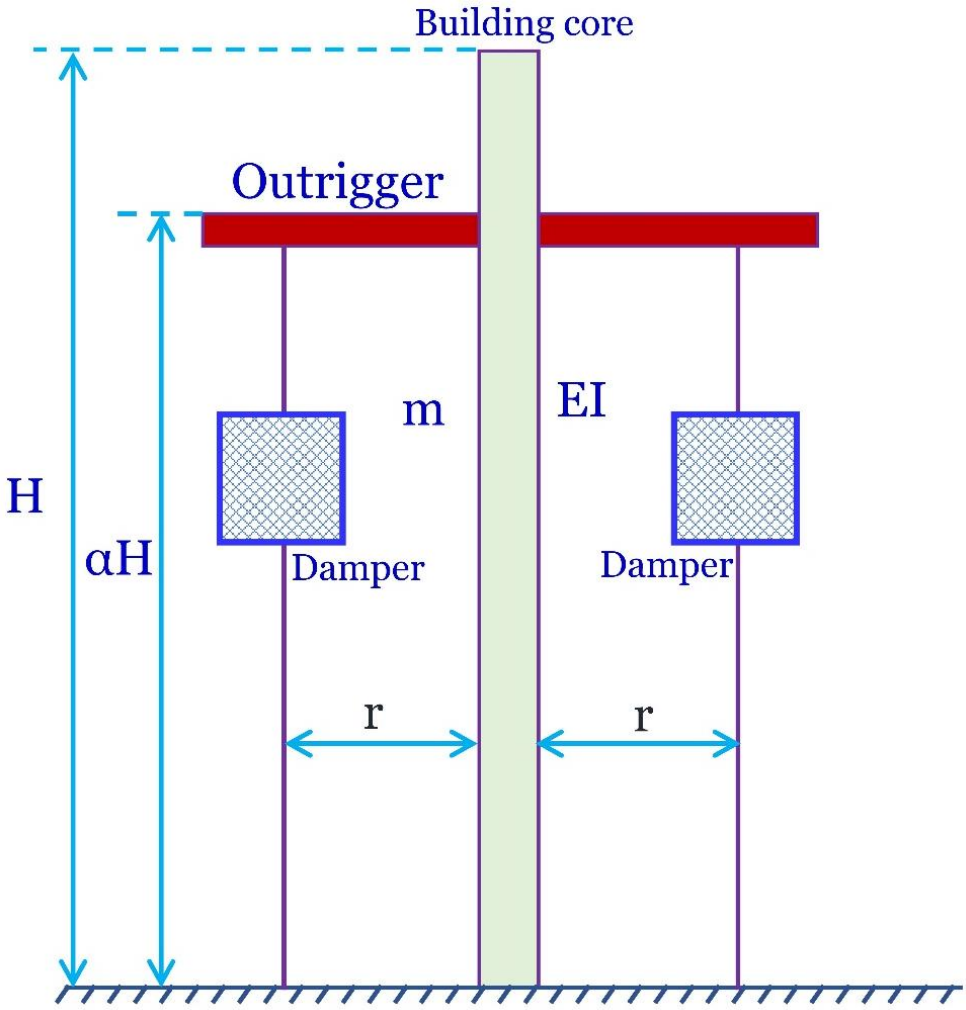
Fig. 2 Comparison between analytical predictions and experimental measurements of the normalized force–displacement response of the negative stiffness device (Nagarajaiah et al. 2022).

3.0 DYNAMIC CHARACTERISTICS OF THE PROPOSED CONTROL DEVICE

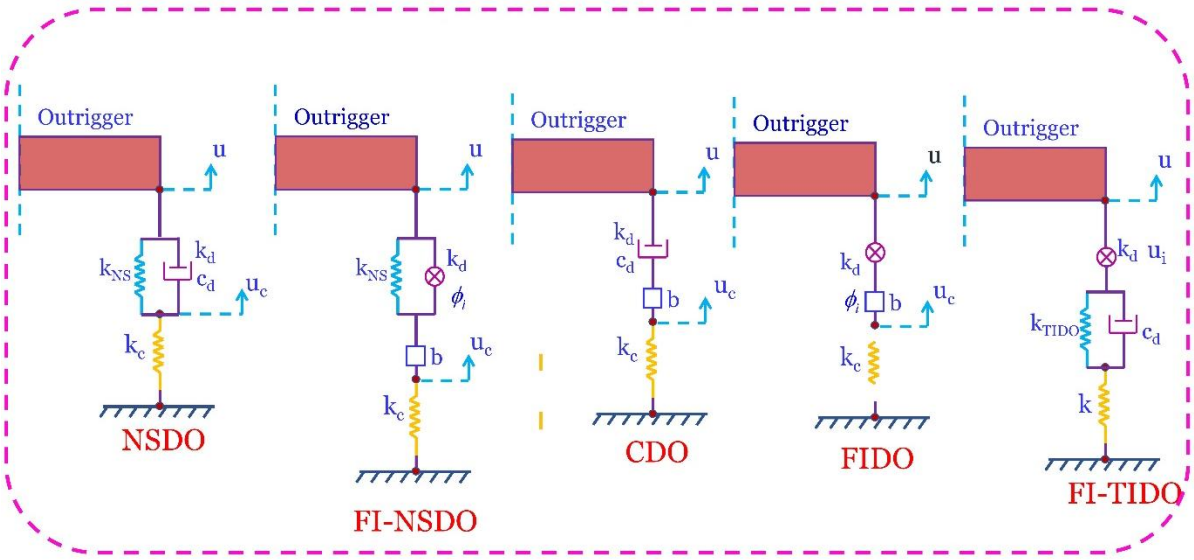
Fig. 3 displays a set of five different damped outrigger systems as a simplified model, where the core tube is considered as a uniform column consisting of distributed mass, bending stiffness, and height (denoted as *m*, *EI*, and *H*,

respectively), as well as a pair of outriggers as a cantilever member at the height $\alpha H(\alpha \in (0,1))$. On the mega column, various types of dampers are connected at the ends of the outrigger. The work reported by Wang et al. (Wang et al. 2020) demonstrated that the outrigger structure can be assumed as an equivalent column stiffness and represented as an equivalent spring with stiffness, k_c. The VD in CDO can be replaced by a FIDO as an FID. In the mega column and at the end of the outrigger connector, the developed FI-NSDO, FID, and NSD are connected in parallel. The force at an outrigger due to FI-NSDO at the end is expressed as:

$$F_d = k_c u_c = k_{NS}(u - u_c) + (k_d + \varphi i)(u - u_c) \quad (8)$$



(a)



(b)

Fig. 3 Analytical model of the proposed tall building equipped with different outrigger control configurations: (a) Structural system; and (b) Control device configurations.

where F_d is the force at the outrigger ends; u_c and k_c are the deformation of the outrigger column and equivalent stiffness, respectively (Wang et al. 2020). The negative stiffness value of NSD is represented as k_{NS}. The parameters for the FID are k_d and φ, respectively. The vertical deformation of the outrigger end is represented as u, and the deformation of NSD with respect to FID is represented as $(u - u_c)$. Eq. (8) is given below by using the Laplace transform as:

$$F_d = k_c \frac{k_{NS} + k_d + \varphi i}{k_c + k_{NS} + k_d + \varphi i} u \tag{9}$$

The force in Eq. (8) is observed independent of frequency ω, where $s = i\omega$ exists in the Laplace variable.

At the end of the outrigger, the resistant moment is expressed as:

$$M_\theta = -2F_d r = -k_\theta \theta \tag{10}$$

where rotational resisting stiffness is expressed as k_θ; rotation at the outrigger is $\theta = \frac{u}{r}$; and the length of the outrigger is represented as L.

$$k_\theta = 2k_c r^2 \frac{k_{NS} + k_d + \varphi i}{k_c + k_{NS} + k_d + \varphi i} \tag{11}$$

Damper stiffness associated with negative stiffness is k_{NS}. The normalized form of the equation is derived based on assumptions of $(k_{NS} + k_d) = \eta k_c, \varphi = \phi k_c, \beta = \frac{EI}{2E_c A_c r^2}, \& \, k_c = \frac{E_c A_c}{\alpha H}$.

$$k_\theta = \frac{EI}{\alpha H \beta} \frac{\eta + \phi i}{1 + \eta + \phi i} \tag{12}$$

From Eq. (12) for $\eta = 0$, the FI-NSDO of rotational stiffness is expressed as

$$k_\theta = \frac{EI}{\alpha H \beta} \frac{\eta + \phi i}{1 + \phi i} \tag{13}$$

In the absence of damper stiffness from Eq. (12), it represents rotational stiffness, which is independent of changes in frequency. Furthermore, the equivalent rotational stiffness for NSDO is already derived from the work by Wang et al. (Wang et al. 2020) as

$$k_\theta = \frac{EI}{\alpha H \beta} \frac{2\lambda^2 c\alpha\beta i + \eta}{1 + 2\lambda^2 c\alpha\beta i + \eta} \tag{14}$$

where $c = c_d r^2 / \left(H\sqrt{mEI}\right)$ is the normalized outrigger damping for VD adopted; and $\lambda^4 = \frac{mH^4}{EI}\omega^2$ is the normalized frequency.

The CDO's equivalent rotational stiffness can be obtained by setting $\eta = 0$ by (Tan et al. 2015):

$$k_\theta = \frac{EI}{\alpha H} \frac{2\lambda^2 ci}{1 + 2\lambda^2 c\alpha\beta i} \tag{15}$$

Equations (14) and (15) contain the term ω, indicating that the behaviour of the Conventional Damping Outrigger (CDO) and the Negative Stiffness Damping Outrigger (NSDO) is frequency-dependent. However, different vibration modes can cause the CDO and NSDO to respond differently. In contrast, Eq. 12 for the CDO and Eq. 13 for the NSDO do not involve ω, implying that the Frequency-Independent Damper (FID) used in the damped outrigger system is frequency-independent, and that the NSD itself is also frequency-independent.

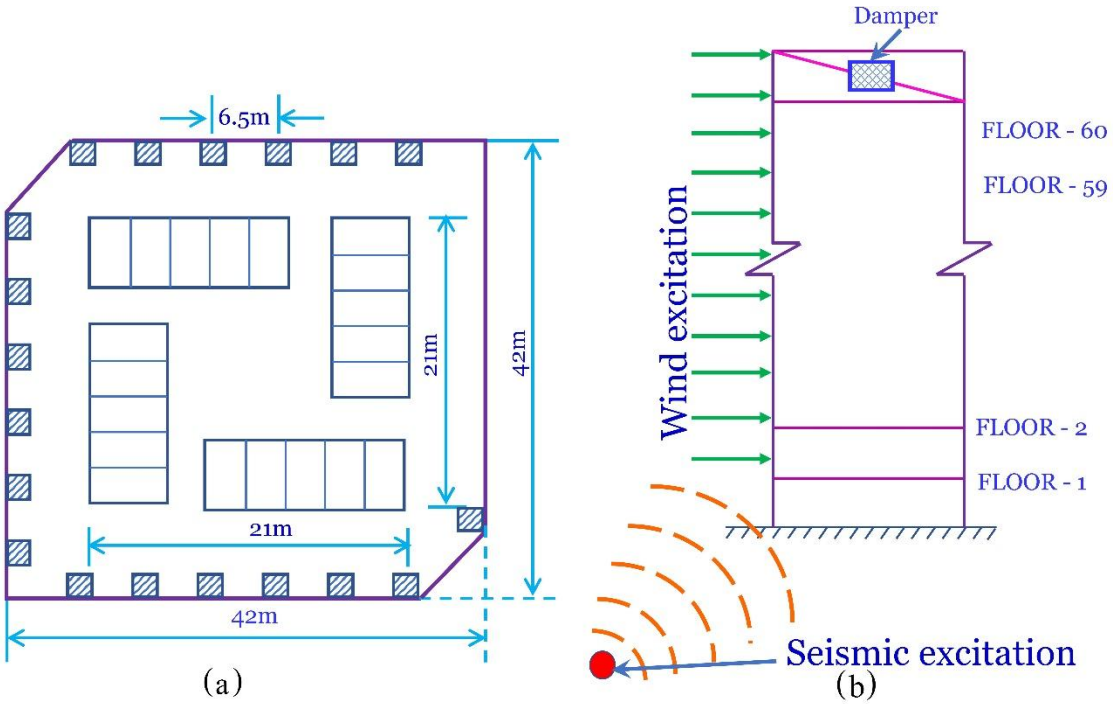


Fig. 4 Benchmark tall building subjected to seismic and crosswind excitations: (a) Plan view; and (b) Elevation.

Fig. 4 illustrates a typical tall building subjected to multiple excitations, including seismic and wind loads. In the present study, a 60-story structural system is considered. The proposed investigation evaluates the performance of tall

structures equipped with various control devices under both seismic and crosswind excitations. The mitigation of structural responses is analysed, and the working principles of the control strategies are presented in the flowchart in Appendix F.

3.1 Governing Equation of Tall Building

Based on Euler-Bernoulli beam theory (Tan et al. 2015; Wang et al. 2020), the tall structure with a damped outrigger pair dynamic equation is expressed as:

$$k_s \begin{bmatrix} cos(\lambda - 2\lambda\alpha)\sin(\lambda) + \cos(\lambda - 2\lambda\alpha)\sin(\lambda) \\ +2\,cos(\lambda\alpha)\sin(\lambda\alpha) + 2\cos(\lambda\alpha)\,sin(\lambda\alpha) \\ +\,cos(\lambda)\sin(\lambda\alpha) + \cos(\lambda)\,sin(\lambda) \\ -2\,cos(\lambda - \lambda\alpha)\sin(\lambda - \lambda\alpha) - 2\cos(\lambda - \lambda\alpha)\,sin(\lambda - \lambda\alpha) \end{bmatrix} + 4[cos(\lambda)\,cosh(\lambda\alpha) + 1] = 0 \quad (16)$$

where

$$k_s = \frac{k_\theta H}{\lambda EI} \quad (17)$$

The FI-NSDO's equivalent stiffness is obtained from Eq. (12) in the above equation.

$$k_s = \frac{1}{\lambda\alpha\beta}\frac{\eta + \phi i}{1 + \eta + \phi i} \quad (18)$$

The solutions of Eq. (16), as follows, are obtained from the Newton Raphson method (Wang et al. 2020):

$$\omega = \sqrt{\frac{\lambda^4 EI}{mH^4}} \quad (19)$$

Following Chen et al. (Chen et al. 2010) the expressions for modal damping ratio and frequency are as follows:

$$\xi = -\frac{Re(i\omega)}{|i\omega|} \quad (20)$$

$$\widetilde{\omega} = |i\omega| \quad (21)$$

The dynamic features of the damped outrigger system, including CDO, NSDO, and FIDO, are obtained from Eqs. (13) to (15) and (16).

3.2 Impact of Outrigger Damping System

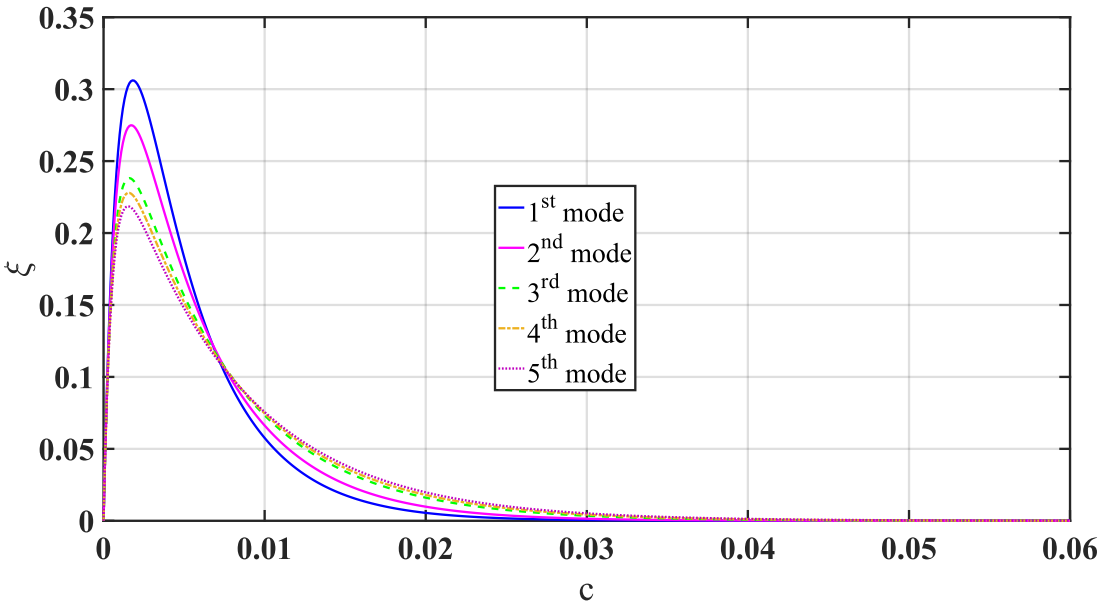
The different dynamic attributes of various damped outrigger systems and the variation in outrigger damping are illustrated in Fig. 5 and 6. At the top of the structure, the parameter α is set to 1.0. Due to the limited stiffness of the outrigger, the maximum achievable damping ratio is constrained. For high-rise structures exhibiting multiple mode shapes, the CDO strategy is limited in that the maximum damping ratio cannot be significantly improved across different damping values. This limitation is evident in Fig. 5(a), where a maximum damping ratio of only 2.5% is observed in the first mode. Additionally, the corresponding outrigger damping coefficient c does not produce higher damping ratios across various damping values. As shown in Fig. 5(a), different vibrational modes under the CDO case achieve their respective maximum damping ratios at specific outrigger damping values. However, due to its frequency-dependent nature, the CDO with variable damping (VD) cannot consistently attain the maximum damping ratio across

all modes. For instance, to achieve a maximum damping ratio of ξ_1=2.89% in the first mode, an outrigger damping value of c=0.024 is required.

For the second mode, a maximum damping ratio of ξ_2=0.79% is achieved. In real-world tall structures subjected to dynamic loads, multiple mode shapes contribute to structural responses. Therefore, damping performance must be evaluated with respect to each mode shape. The proposed NSDO system improves both stiffness and damping ratios across different vibrational modes, thus addressing the frequency-dependence limitation inherent in conventional damped outrigger systems. Specifically, the damping ratio of the first mode increases from 2.88% (CDO) to 24.32% using the NSDO system, requiring only an outrigger damping of c=0.004, which represents an 84.5% improvement over the CDO, as shown in Fig. 5(b). Similarly, the TIDO system improves the first-mode damping ratio from 3.28% to 22.45% using an outrigger damping of c=0.0035, reflecting a 73.5% enhancement over the CDO, as seen in Fig. 5(c). However, for achieving efficient dynamic performance across multiple vibration modes, especially in trade-off design scenarios, the NSDO system plays a crucial role (Wang et al. 2021).

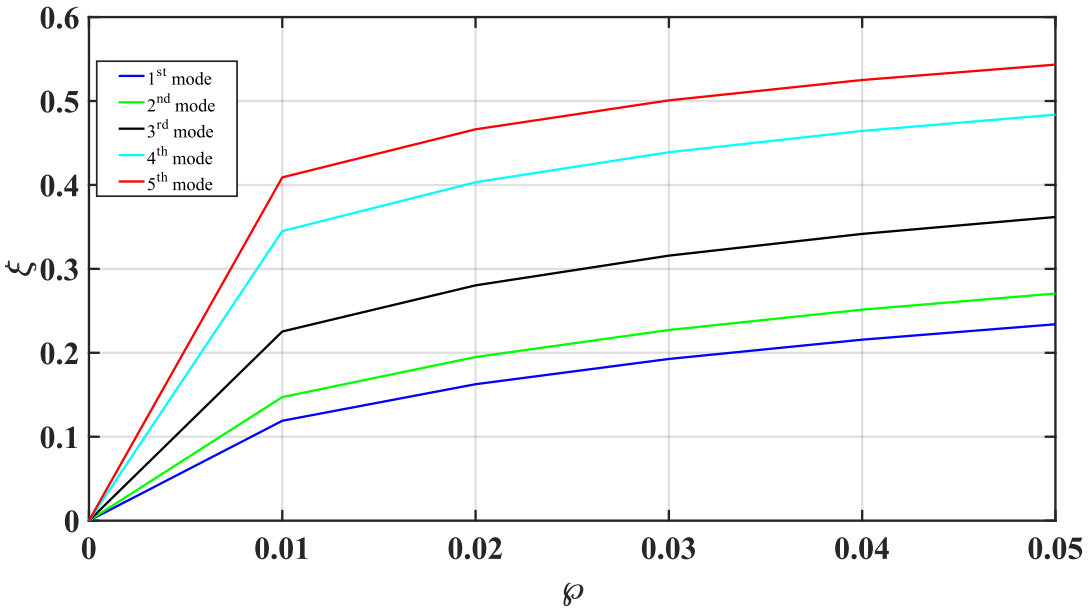
The first five modes and their corresponding frequencies for the various damped outrigger systems are presented in Fig. 6. Five modes are considered in the present study, as they are significant for understanding the dynamic performance of tall structures and for determining the modal participation factors. As damping increases, the associated modal frequency initially increases and then plateaus (Chen et al. 2010). A clear distinction exists between frequency-dependent damped outriggers (CDO and NSDO) and frequency-independent systems (FID, FI-NSDO, and FI-TIDO). In higher vibration modes, the frequencies of CDO and NSDO converge to those of the frequency-independent systems, enhancing negative stiffness behaviour in the damper and promoting frequency-independence.

The observed behaviour indicates that the frequency-independent hysteretic component governs the energy dissipation mechanism rather than the excitation frequency. Consequently, the proposed FI-TIDO maintains stable modal characteristics over a broad frequency range, reducing sensitivity to modal frequency variations that typically affect conventional frequency-dependent outrigger systems.

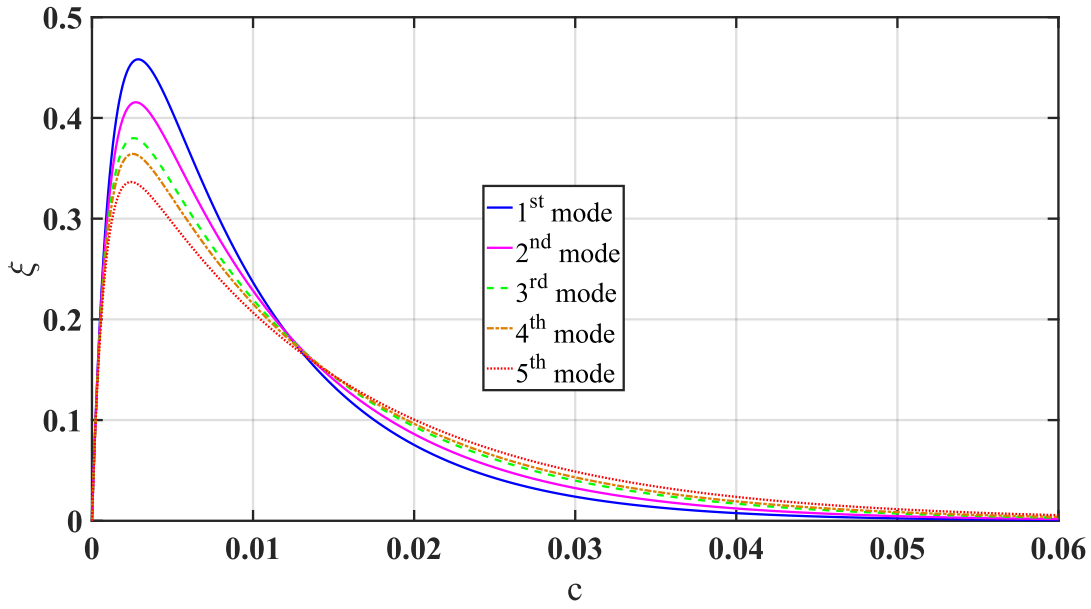

0.35
0.3
0.25
0.2
0.15
0.1
0.05
0
ξ
0
0.01
0.02
0.03
0.04
0.05
0.06
c
1st mode
2nd mode
3rd mode
4th mode
5th mode

256

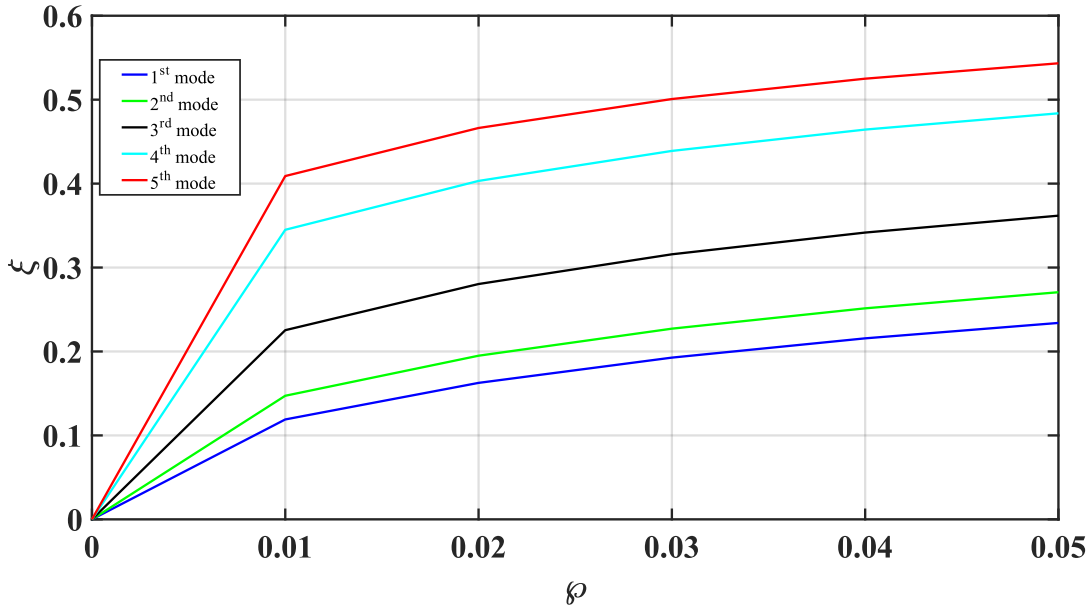
(a)


0.6
0.5
0.4
0.3
0.2
0.1
0
ξ
0
0.01
0.02
0.03
0.04
0.05
℘
1st mode
2nd mode
3rd mode
4th mode
5th mode

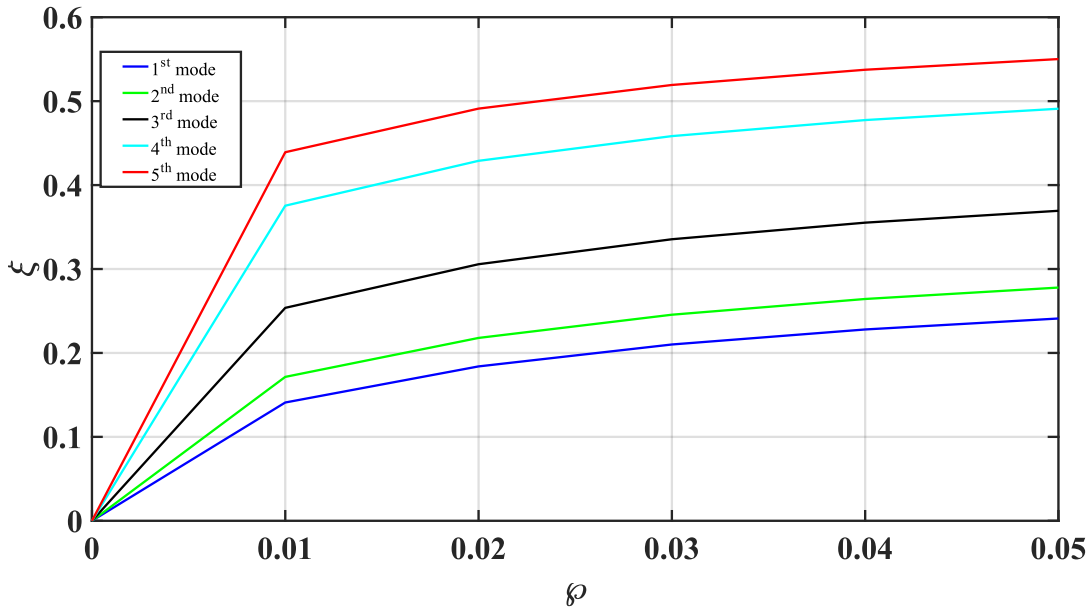
(b)


0.5
0.4
0.3
0.2
0.1
0
ξ
0
0.01
0.02
0.03
0.04
0.05
0.06
c
1st mode
2nd mode
3rd mode
4th mode
5th mode

(c)

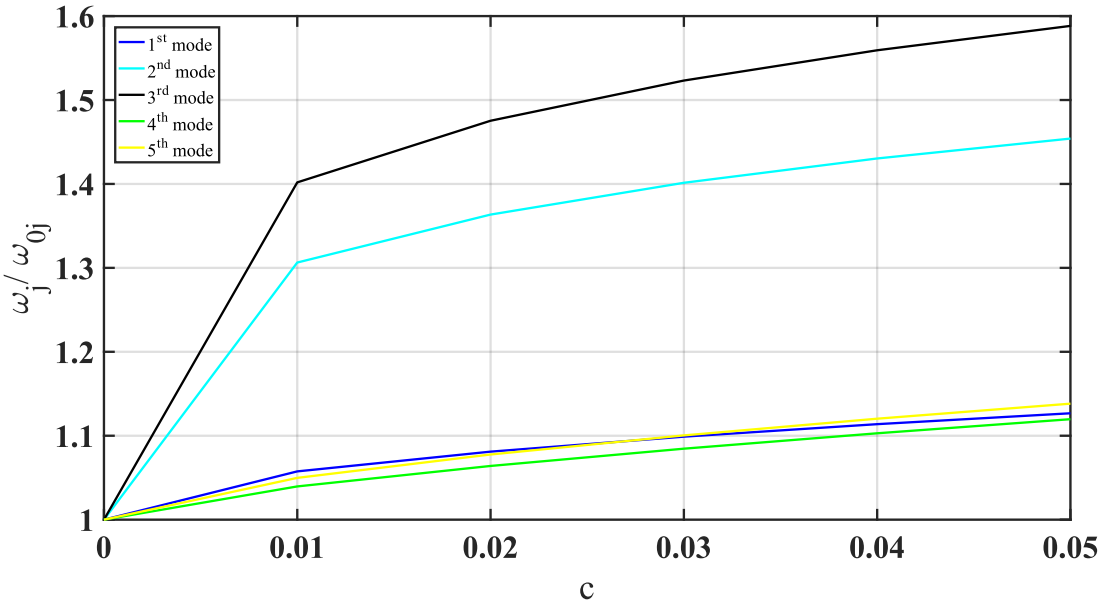

0.6
0.5
0.4
0.3
0.2
0.1
0
ξ
0
0.01
0.02
0.03
0.04
0.05
℘
1st mode
2nd mode
3rd mode
4th mode
5th mode

(d)

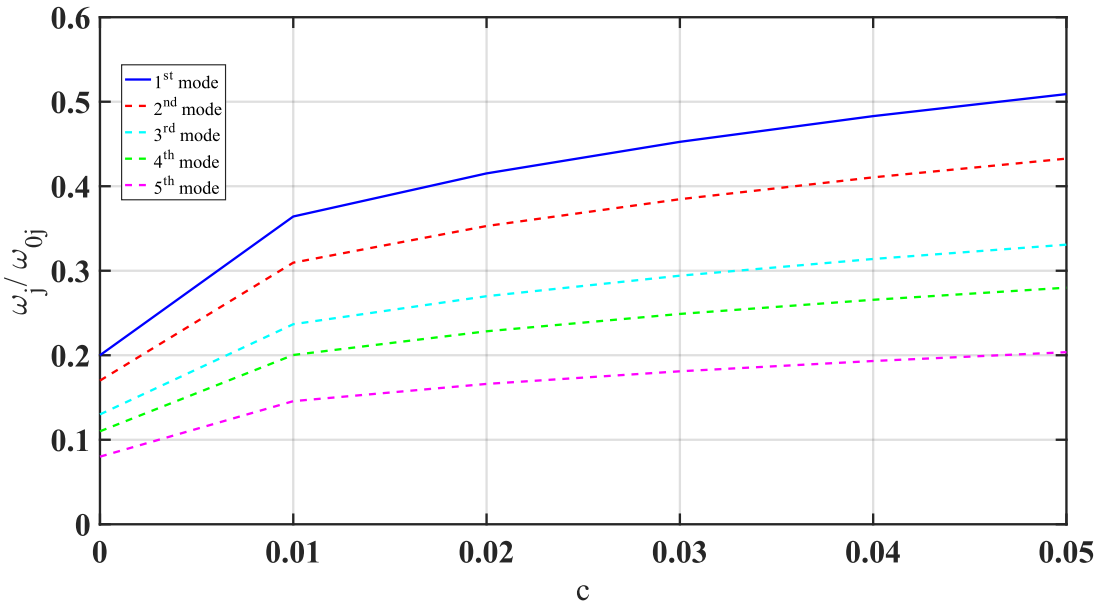


(e)

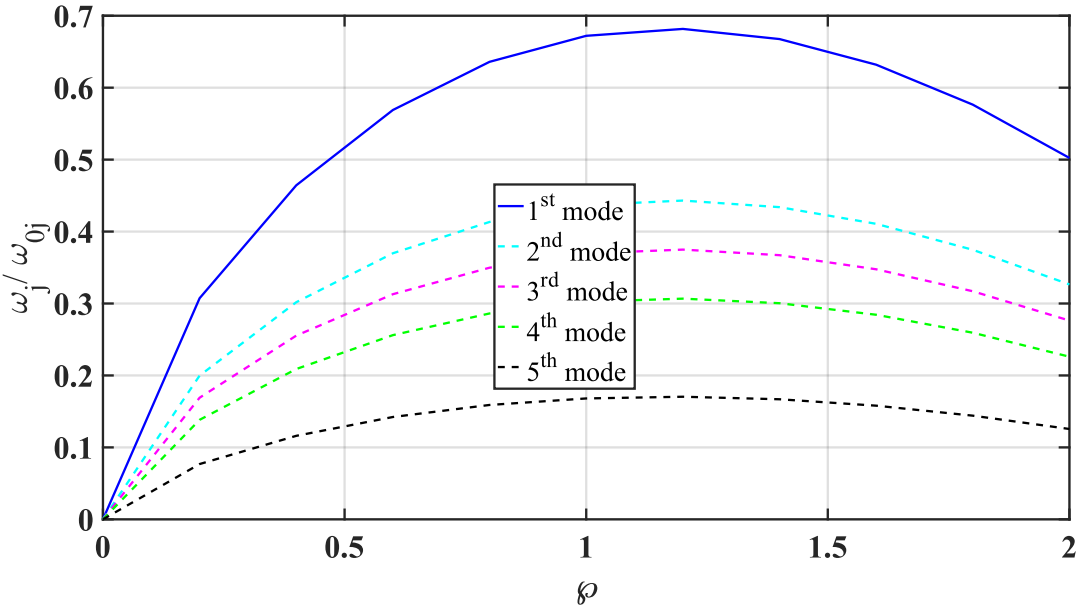
Fig. 5 Variation of modal damping ratios of the first five vibration modes for different outrigger systems with varying outrigger damping: (a) CDO; (b) NSDO; (c) FIDO; (d) FI-NSDO; and (e) FI-TIDO.



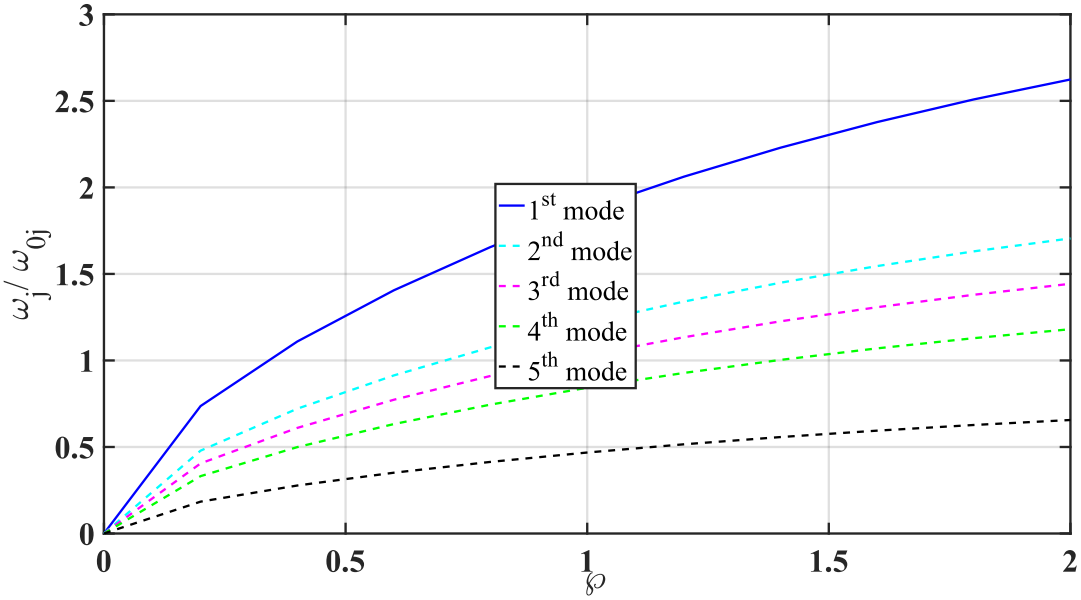
(a)


0.6
0.5
0.4
0.3
0.2
0.1
0
0
0.01
0.02
0.03
0.04
0.05
ω_j / ω_{0j}
c
1st mode
2nd mode
3rd mode
4th mode
5th mode

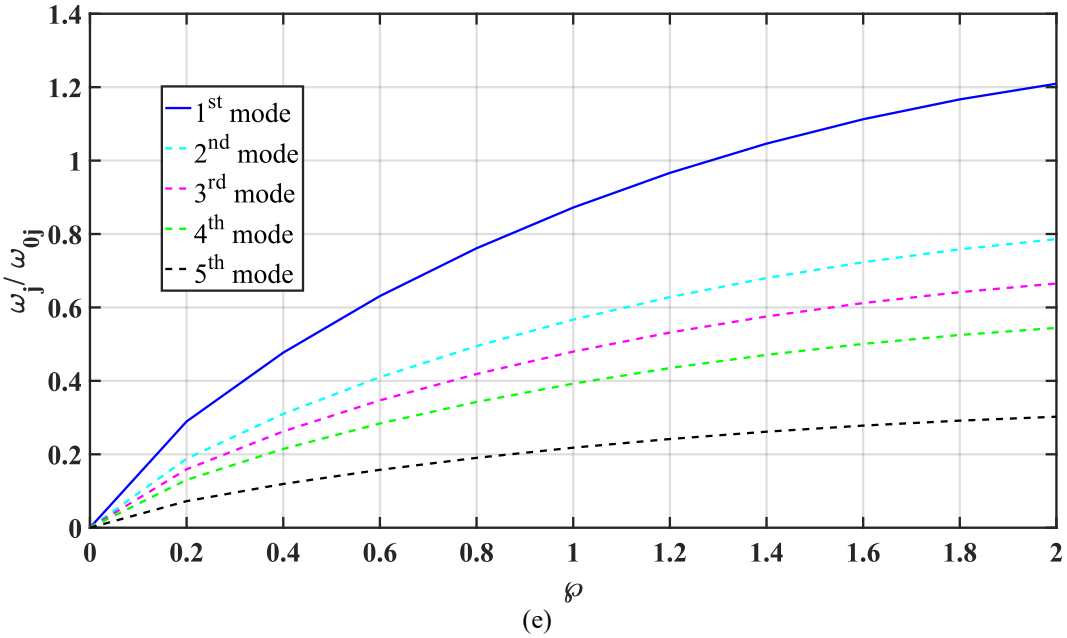
(b)


0.7
0.6
0.5
0.4
0.3
0.2
0.1
0
0
0.5
1
1.5
2
ω_j / ω_{0j}
℘
1st mode
2nd mode
3rd mode
4th mode
5th mode

(c)



(d)



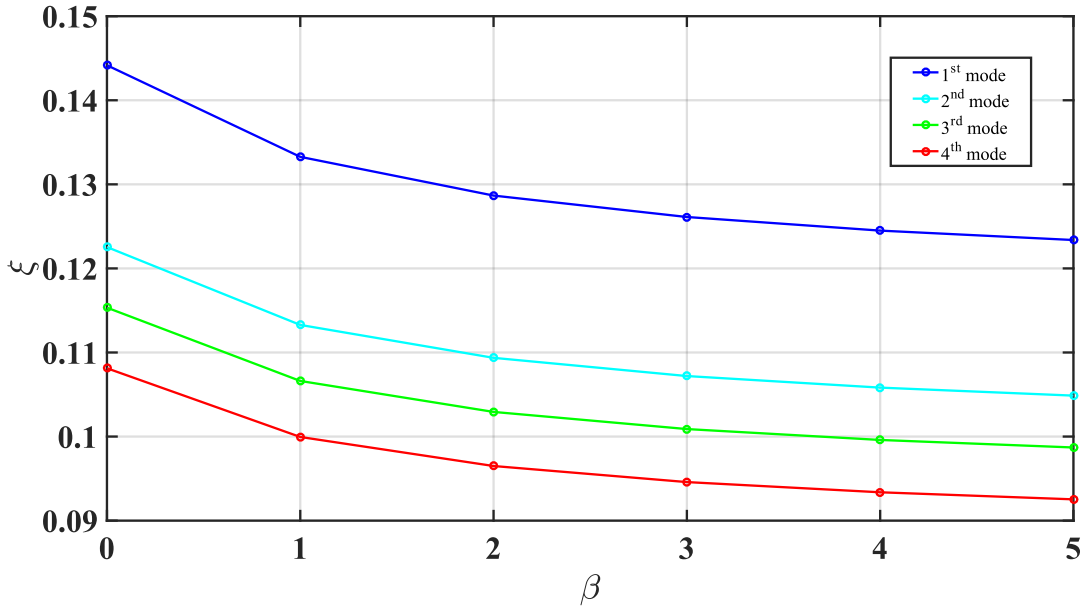
(e)

Fig. 6 Variation of modal frequencies of the first five vibration modes for different outrigger systems with varying outrigger damping: (a) CDO; (b) NSDO; (c) FIDO; (d) FI-NSDO; and (e) FI-TIDO.

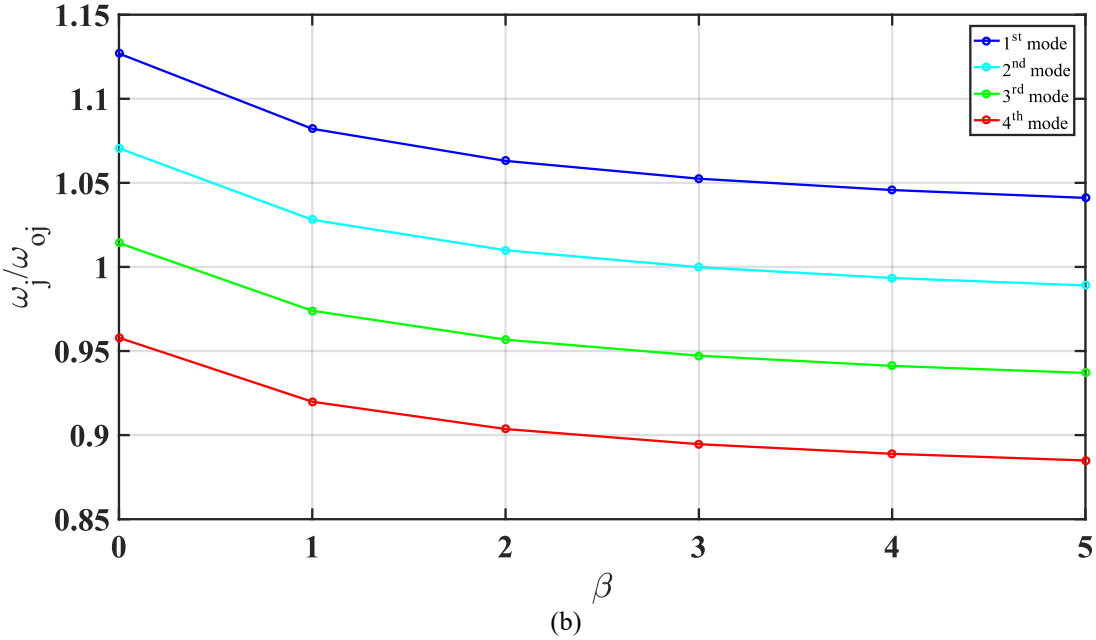
3.3 Impact of Tuned Inerter Damped Outrigger/Column Stiffness

Key parameters of outrigger/column, that include stiffness (β) and negative stiffness (η), achieve the maximum damping ratio of CDO and NSDO. The dynamic characteristics of FI-TIDO with different values of negative stiffness and outrigger column stiffness are shown in Fig. 7 and 8, respectively. As the damping ratio (ξ) increases, the corresponding β value decreases. The increase in modal damping is attributed to the combined action of inerter amplification and frequency-independent hysteretic damping, which enhances energy dissipation without relying on

resonance-based tuning. Consequently, the proposed FI-TIDO provides effective vibration mitigation across multiple structural modes, whereas the performance of conventional damped outriggers remains more sensitive to changes in structural frequency. However, for different mode shapes with peak multi excitation responses, the FI-TIDO plays a vital role, as observed in Fig. 7. Maximum damping ratio attained due to the negative stiffness of FI-NSDO is shown in Fig. 8.



(a)



(b)

Fig. 7 Influence of outrigger stiffness on the dynamic characteristics of the FI-TIDO system: (a) Maximum modal damping ratio; and (b) Corresponding modal frequency ratio.

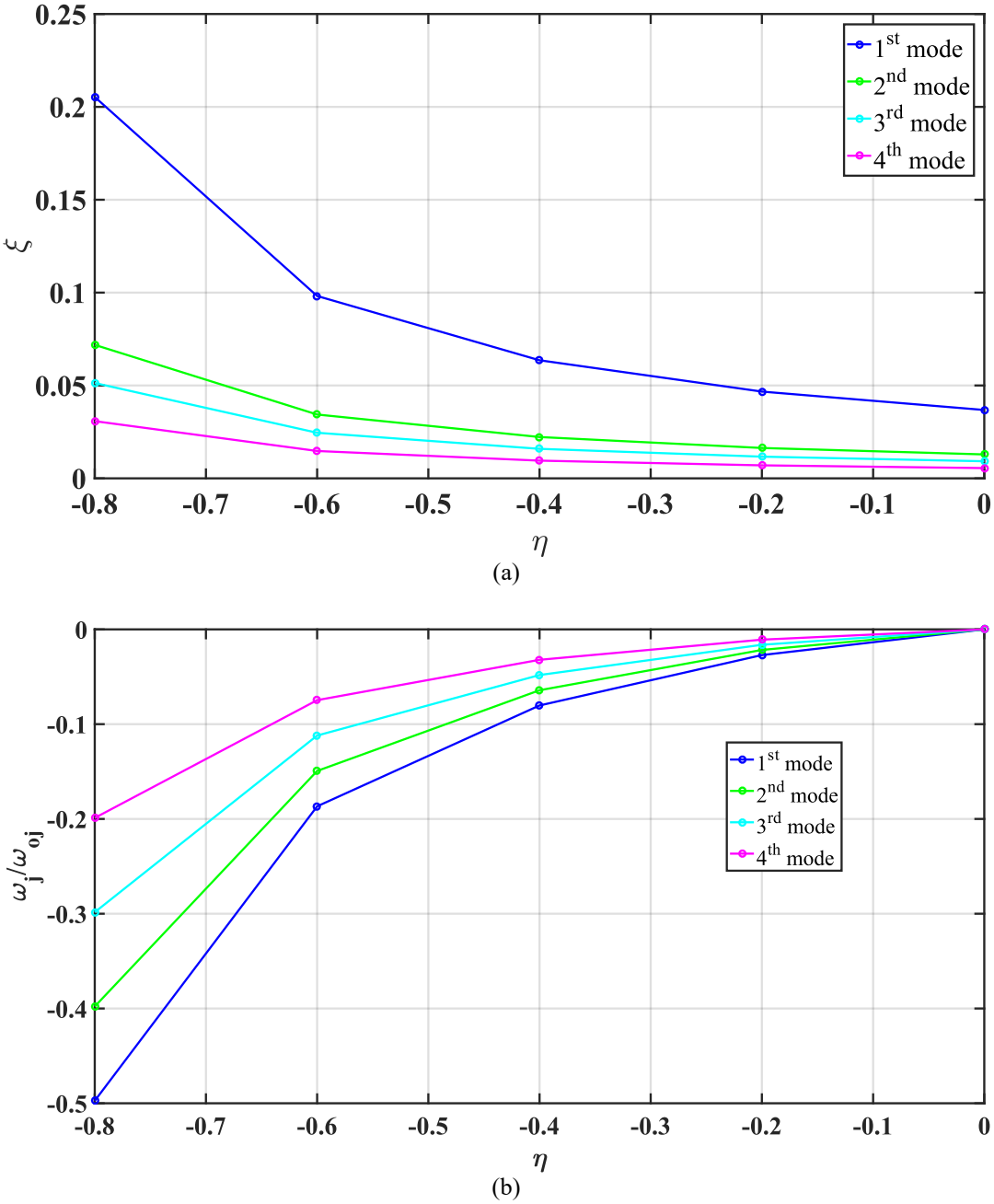
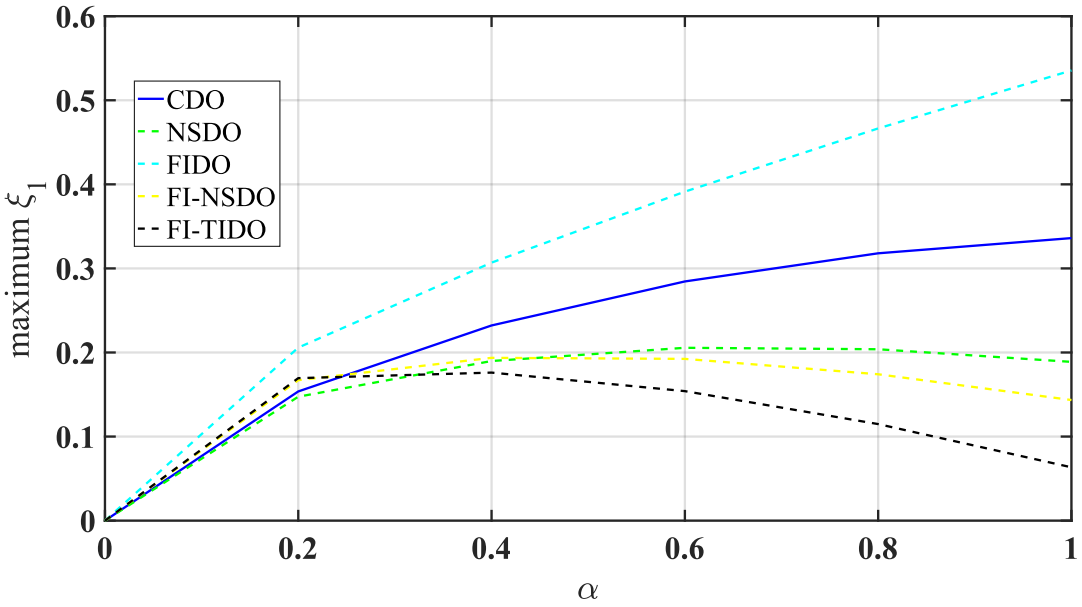


Fig. 8 Influence of negative stiffness on the dynamic characteristics of the FI-TIDO system (β = 5): (a) Peak modal damping ratio; and (b) Corresponding modal frequency ratio.

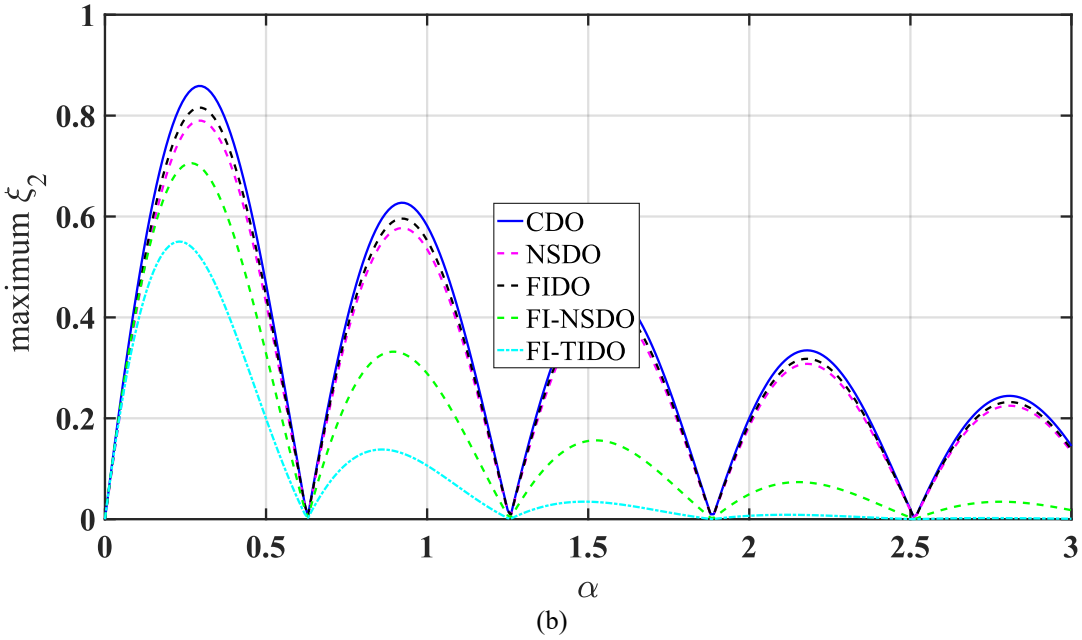
3.4 Impact of Outrigger Position

During the design of any tall structure with the outrigger, the position of an outrigger is considered as the main parameter. The different peak modal damping ratios and their outrigger positions are depicted in Fig. 9. The five damped outrigger system exhibits similar trends with respect to the position of an outrigger. The results indicate that the higher damping occurs in tall structures at mid part ($\alpha = 0.59$) at peak modes, as shown in the second mode. In addition, it is observed that the damping ratio decreases at higher modes with different outrigger systems. Detailed

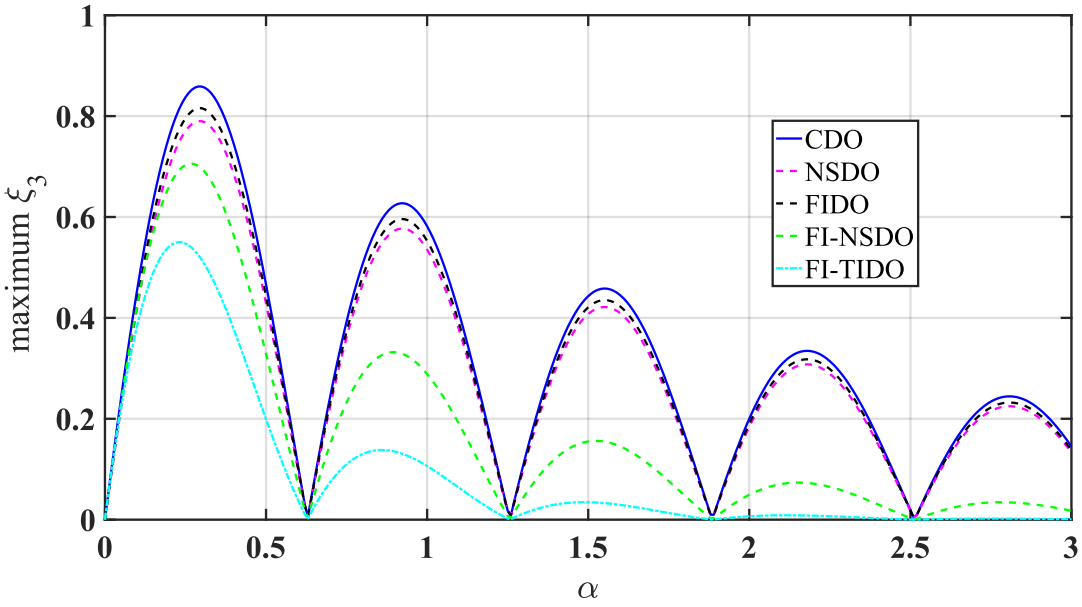
information on the position of the outrigger can be found elsewhere (Wang et al. 2023). Table 1 presents the optimum parameter of the outrigger position and the relating damping ratio of FI-TIDO. It can be concluded that the outrigger damper can be better positioned at the top of the tall structure as compared to the bottom for vibration mitigation of the structure.



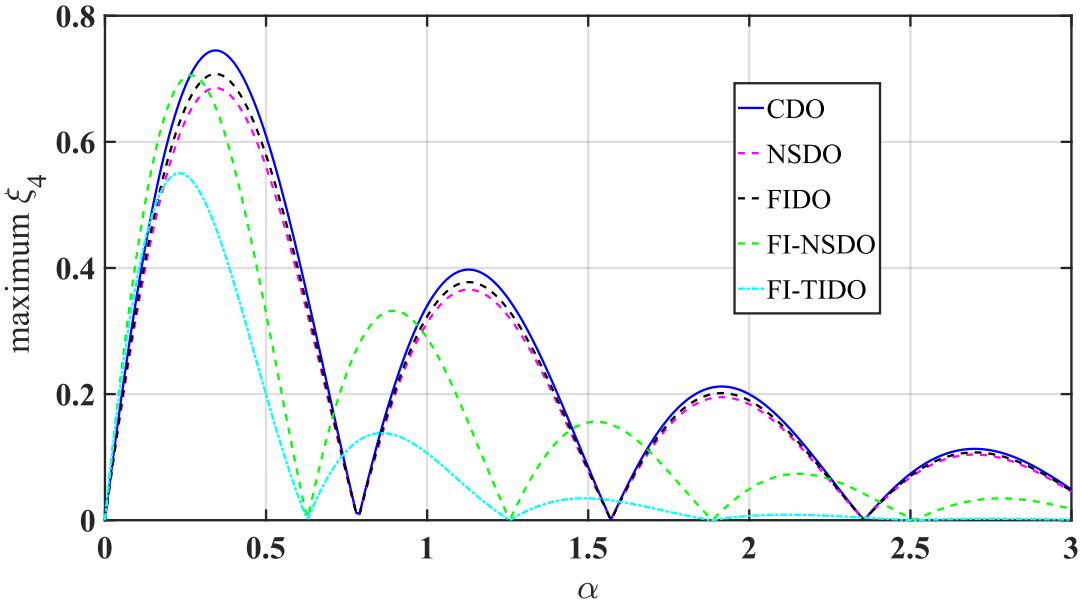
(a)



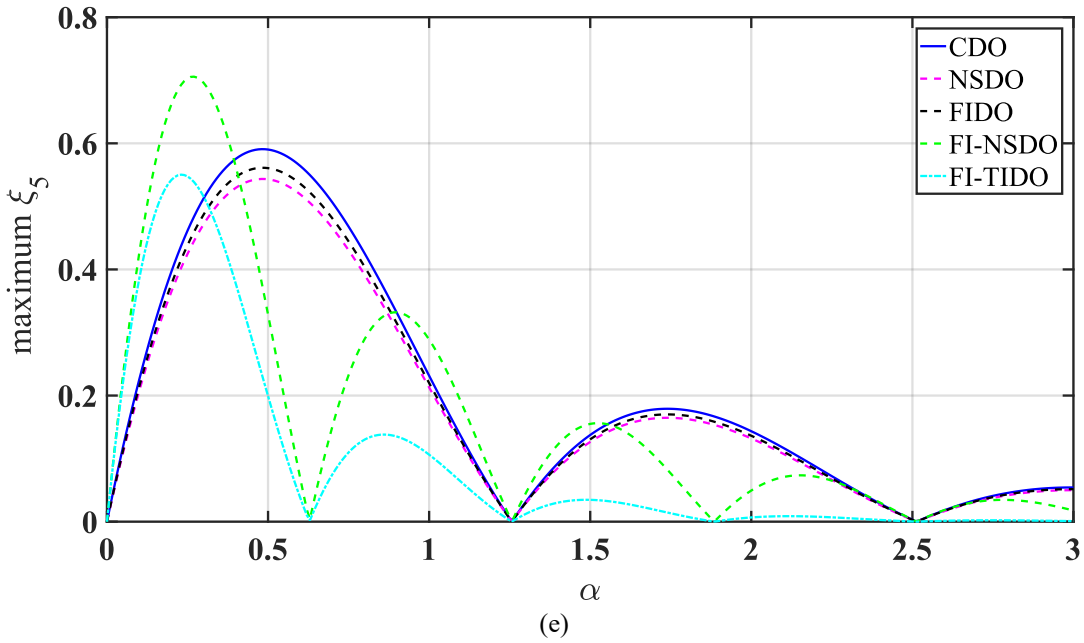
(b)


maximum ξ_3
α
CDO
NSDO
FIDO
FI-NSDO
FI-TIDO

(c)


maximum ξ_4
α
CDO
NSDO
FIDO
FI-NSDO
FI-TIDO

(d)



(e)

Fig. 9 Influence of outrigger location on the maximum modal damping ratios of different outrigger systems: (a) First mode; (b) Second mode; (c) Third mode; (d) Fourth mode; and (e) Fifth mode.

Table 1 Optimum position of the outrigger and the related damping ratio of FI-TIDO with different mode shape.

Outrigger position	α	$\xi_1(\%)$	$\xi_2(\%)$	$\xi_3(\%)$	$\xi_4(\%)$
First mode	0.55	24.255	0.185	1.325	0.035
Second mode	0.12	12.852	6.325	3.345	1.625
	0.94	19.925	4.485	1.345	0.585
Third mode	0.07	9.256	5.728	3.772	2.625
	0.48	23.725	0.0065	1.425	0.038
	0.98	19.085	4.402	1.408	0.692
Fourth mode	0.045	6.928	4.935	3.678	2.745
	0.38	22.525	1.302	0.362	1.006
	0.66	23.178	1.811	0.185	0.525
	0.99	18.825	4.356	1.425	0.699

Table 2 presents a comparative study of frequency-dependent and frequency-independent TIDO systems, analysing their dynamic performance across various damping ratios and outrigger positions. The results indicate that the frequency-dependent TIDO consistently yields lower damping ratios compared to the frequency-independent TIDO. This discrepancy arises because the damping performance of the frequency-dependent TIDO is strongly influenced by its tuning to a specific structural frequency, which limits its effectiveness across multiple modes. In contrast, the frequency-independent TIDO maintains consistent dynamic performance without requiring resonance-based tuning, making it more effective for multimodal vibration control.

Table 2 Comparative Investigation of Optimal Outrigger Positions and Corresponding Damping Ratios for Frequency-Independent (FI-TIDO) and Frequency-Dependent (TIDO) Systems Across Different Mode Shapes

Outrigger position	α	$\xi_1(\%)$	$\xi_1^*(\%)$	$\xi_2(\%)$	$\xi_2^*(\%)$	$\xi_3(\%)$	$\xi_3^*(\%)$	$\xi_4(\%)$	$\xi_4^*(\%)$
First mode	0.550	24.255	21.232	0.1850	0.1750	1.325	1.258	0.035	0.0295
Second mode	0.120	12.852	10.952	6.3250	5.9850	3.345	3.258	1.625	1.5450
	0.940	19.925	1.7245	4.4850	4.3250	1.345	1.258	0.585	0.5450
Third mode	0.070	9.2560	7.3580	5.7280	5.4520	3.772	3.625	2.625	2.5850
	0.480	23.725	21.524	0.0065	0.0058	1.425	1.325	0.038	0.0360
	0.980	19.085	17.065	4.4020	4.3250	1.408	1.385	0.692	0.6950
Fourth mode	0.045	6.9280	5.9850	4.9350	4.7850	3.678	3.585	2.745	2.6540
	0.380	22.525	21.225	1.3020	1.1250	0.362	0.325	1.006	1.0001
	0.660	23.178	22.385	1.8110	1.7250	0.185	0.175	0.525	0.4850
	0.990	18.825	17.958	4.3560	4.1250	1.425	1.325	0.699	0.5850

* Represents the Frequency-dependent parameter

4.0 DYNAMIC PERFORMANCE OF THE PROPOSED SYSTEMS UNDER SEISMIC EXCITATION

The previous sections demonstrated the dynamic analysis for various damped outrigger systems and concluded that the proposed FI-TIDO can significantly improve the damping ratio with respect to different modes. This corresponds to the proposed frequency-independent feature as well as the improved frequency-independent tuned inerter damped outrigger technique. The investigation of the external excitation, i.e., seismic load, is necessary for higher-mode effects with both frequency domain analysis and time domain analysis.

The seismic responses of finite element models for various damped outrigger systems are developed in this section. The tall structure with a dynamic equation equipped with different damped outrigger systems under seismic ground motion is given as:

$$M\ddot{y} + C\dot{y} + Ky + \psi M_\theta = -M\delta\ddot{x}_g \tag{22}$$

where mass, damping, and stiffness of the structure are M, C, and K, respectively; displacement in the transverse direction and rotational deformation of each story in vector form is y; ground excitation is $\ddot{x}_g$; earthquake excitation in vector form is δ; resisting moment obtained from damped outrigger is M_θ; and position vector of the outrigger is ψ.

The tall structure at the outrigger position of rotation is expressed as:

$$\theta = \psi^T y; \dot{\theta} = \psi^T \dot{y} \tag{23}$$

The vertical displacement of the outrigger end is represented as:

$$u = \theta r = \psi^T y r \tag{24}$$

Eq. (23) is substituting in Eq. (9) to obtain the dynamic equation of a tall structure equipped with FI-TIDO, as follows:

$$M\ddot{y} + C\dot{y} + Ky + \frac{3r^2 k_c(\eta + \phi i)}{1 + \eta + \phi i}\psi\psi^T y = -M\delta\ddot{x}_g \tag{25}$$

$$M\ddot{y} + C\dot{y} + \widetilde{K}y = -M\delta\ddot{x}_g \tag{26}$$

where $\widetilde{K}= K +\frac{2r^2 k_c(\eta+\phi i)}{1+\eta+\phi i}\psi\psi^T$.

Eq. (25) is rewritten and expressed in state-space form as:

$$\begin{aligned} \dot{Y}_S &= A_S Y_S + B_S\ddot{x}_g \\ P_S &= C_S Y_S + D_S\ddot{x}_g \end{aligned} \tag{27}$$

where

$$Y_S = \begin{bmatrix}\dot{y}\\ y\end{bmatrix}; A_S = \begin{bmatrix}-M^{-1}C & -M^{-1}\widetilde{K}\\ I & 0\end{bmatrix}; B_S = \begin{bmatrix}-M\delta\\ 0\end{bmatrix} \tag{28}$$

P_S is the output variable vector, and the output matrices are C_S and D_S. The transfer function is determined as follows:

$$G(\omega) = \left[-M\omega^2 + Ci\omega + \widetilde{K}\right]^{-1} \tag{29}$$

The dynamic equation of a tall structure with TIDO is determined by setting $\eta = 0$. For the detailed solutions for the state-space expressions for CDO, it is advisable (Sun et al. 2021).

In this section, the St. Francis Shangri-La Palace - a 60-story building with a height of 210 meters—is examined, as it is the first tall structure to incorporate a damped outrigger system. The key parameters used in this study include the stiffness of the core tube (EI = 1.828×10^{13} N·m²), the mass distributed across all floors (m = 9.0308×10^4 kg/m), and the length of the outrigger (r = 4 m). Further details about the structure can be found in (Smith and Willford 2007). As discussed in the previous section, higher damping ratios are achieved using FI-NSDO and FI-TIDO compared to CDO and FIDO, emphasizing the distinction between the frequency-independent and frequency-dependent behaviour of NSDO. The optimal parameters for the tall structure are summarized in Table 3.

Table 3 Optimally designed parameters of TIDO and FI-TIDO.

Parameters	TIDO (1st mode)	TIDO (2nd mode)	FI-TIDO
Outrigger damping	c = 0.0034	c = 0.0008	c = 0.15
Tuned inerter stiffness	$\eta = -0.65$	$\eta = -0.68$	$\eta = -0.74$
Column/outrigger stiffness	$\beta = 6.0$	$\beta = 6.0$	$\beta = 6.0$
Outrigger position	$\alpha = 1.0$	$\alpha = 1.0$	$\alpha = 1.0$

4.1 Frequency Domain Analysis

Five configurations of the structure are considered in this study:

(a) A tall structure with an uncontrolled damped outrigger,

(b) The first mode of vibration for an optimally designed NSDO,

(c) The second mode of vibration for an optimally designed NSDO,

(d) Multiple vibration modes for an optimally designed NSDO, and

(e) Multiple vibration modes for an optimally designed TIDO.

4.2 Frequency Domain Analysis

The present model considers the stochastic process as an input parameter for performing frequency domain analysis. The Clough and Penzien model are used in the present study as a filtered Gaussian white-noise process. It is expressed as a power spectral density (PSD), as shown below (Clough and Penzien 1975):

$$S(\omega) = \frac{1 + 4\xi_g^2 \left(\frac{\omega}{\omega_g}\right)^2}{\left\{1 - \left(\frac{\omega}{\omega_g}\right)^2\right\}^2 + 4\xi_g^2 \left(\frac{\omega}{\omega_g}\right)^2} \cdot \frac{\left(\frac{\omega}{\omega_f}\right)^4}{\left\{1 - \left(\frac{\omega}{\omega_f}\right)^2\right\}^2 + 4\xi_f^2 \left(\frac{\omega}{\omega_f}\right)^2} S_0 \tag{30}$$

where the soil parameters (frequencies and damping ratios) are represented as ω_f, ξ_f, ω_g and ξ_g, respectively. The intensity of the white noise process is expressed as S_0.

The earthquake excitation for the PSD matrix is represented as:

$$S_{EQ}(\omega) = M\delta^T S(\omega)\delta \tag{31}$$

The displacement and acceleration responses of PSD are given as:

$$S_Y(\omega) = G(\omega)^* S_{EQ}(\omega) G(\omega) \tag{32}$$

$$S_{\ddot{Y}}(\omega) = \omega^4 S_Y(\omega) \tag{33}$$

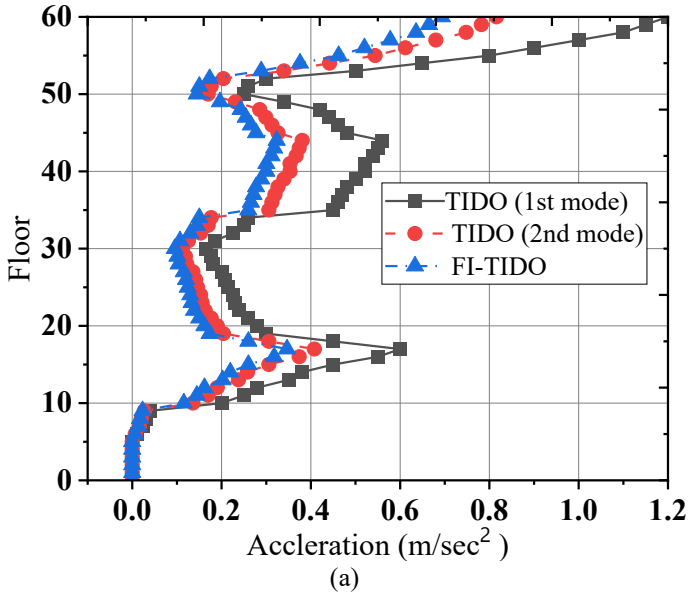
The root mean square value for seismic response is determined by the following integration:

$$\sigma_{y_j} = \left[\int_0^\infty S_Y^j(\omega) d\omega\right]^{\frac{1}{2}}, \sigma_{y_j} = \left[\int_0^\infty S_{\ddot{Y}}^j(\omega) d\omega\right]^{\frac{1}{2}} \tag{34}$$

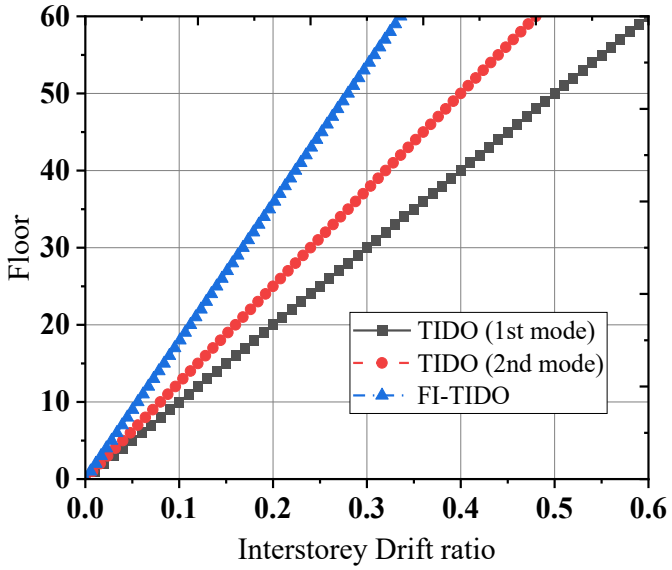
The dynamic performance of a tall structure, supplied with NSDO and FI TIDO, is obtained using the frequency domain analysis under seismic response is represented in Fig. 10 and 11, respectively. It is observed that the first mode of NSDO design outperforms the second mode for interstory drifts by a reduction of 32.5% compared to the design for NSDO of the second mode. However, the simultaneous reduction of both story drift and acceleration response in the first mode for minimum frequency is dependent on TIDO. Moreover, the NSDO cannot attain the maximum damping ratio in all modes, as shown in Fig. 10. Multimodal vibration control FI-TIDO performs better than those of the NSDO and TIDO with respect to controlling story drift response of 23.45% as compared to the first mode of NSDO response. Table 4 shows the optimally designed parameters of FI-NSDO and FI-TIDO. The improved performance is primarily attributed to the combined effects of inerter action, frequency-independent hysteretic damping, and negative stiffness. While conventional outrigger systems achieve vibration reduction mainly through resonance-based tuning, the proposed FI-TIDO dissipates energy over a wider frequency range, thereby providing more consistent multimodal vibration mitigation under both seismic and crosswind excitations.

Tall structures exhibit significant higher-mode contributions to the acceleration response under seismic excitation, as shown in Fig. 11. Both the NSDO and FI-TIDO systems effectively reduce the response amplitudes; however, the

proposed FI-TIDO provides improved vibration suppression over multiple vibration modes. While the conventional TIDO exhibits enhanced performance primarily near its tuned mode, the FI-TIDO effectively suppresses responses across all significant modes. The reduction in the power spectral density demonstrates that the proposed frequency-independent damping mechanism suppresses structural response over a broad range of excitation frequencies rather than at a single resonance frequency. This characteristic is particularly advantageous for tall buildings, where several vibration modes contribute simultaneously to the overall seismic response.



(a)



(b)

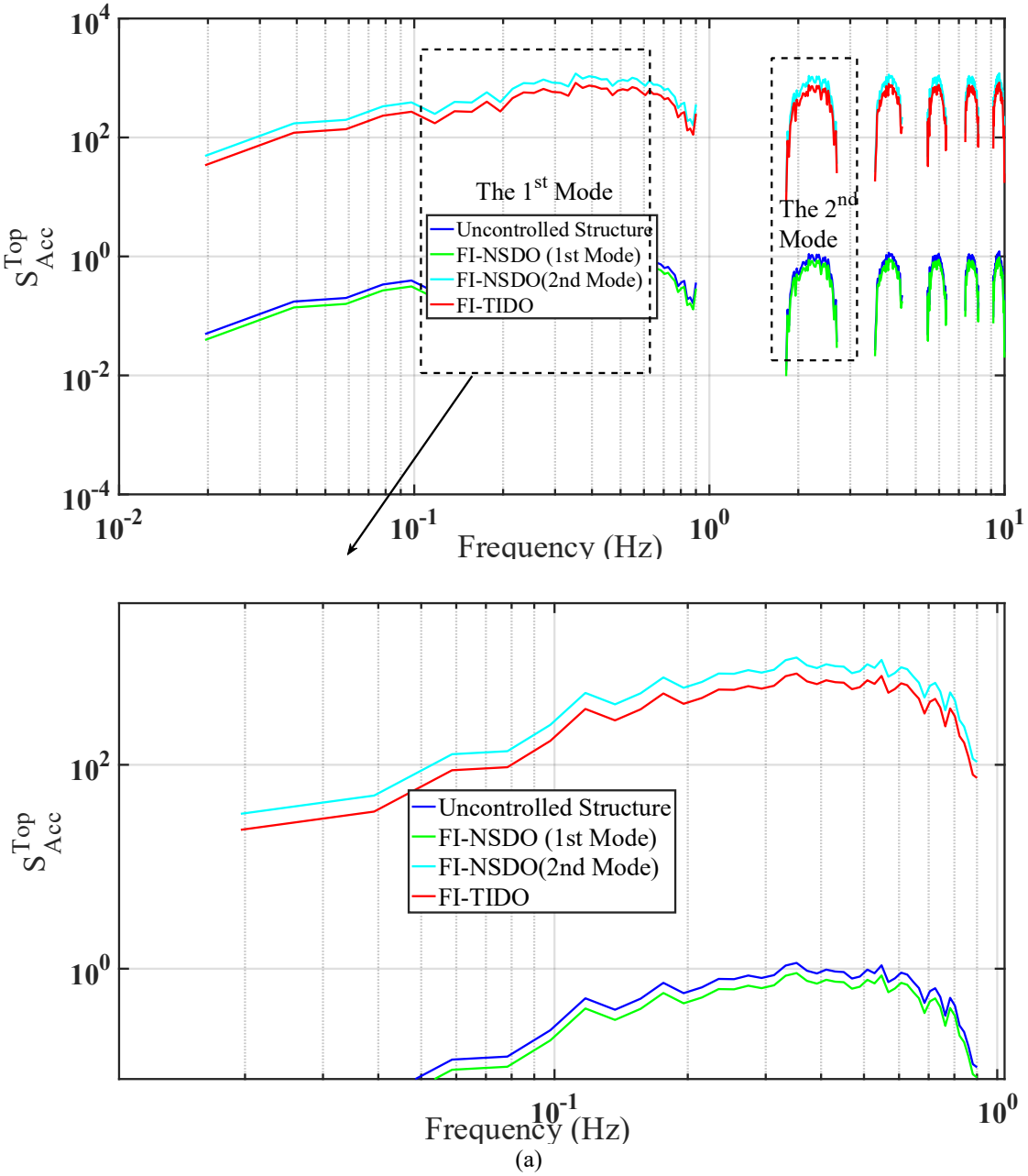
Fig. 10 Seismic performance of 60-story benchmark building fortified with TIDO and FI-TIDO using frequency domain analysis: (a) Acceleration; and (b) Interstory drift for Cape Mendocino time-history analysis.

.

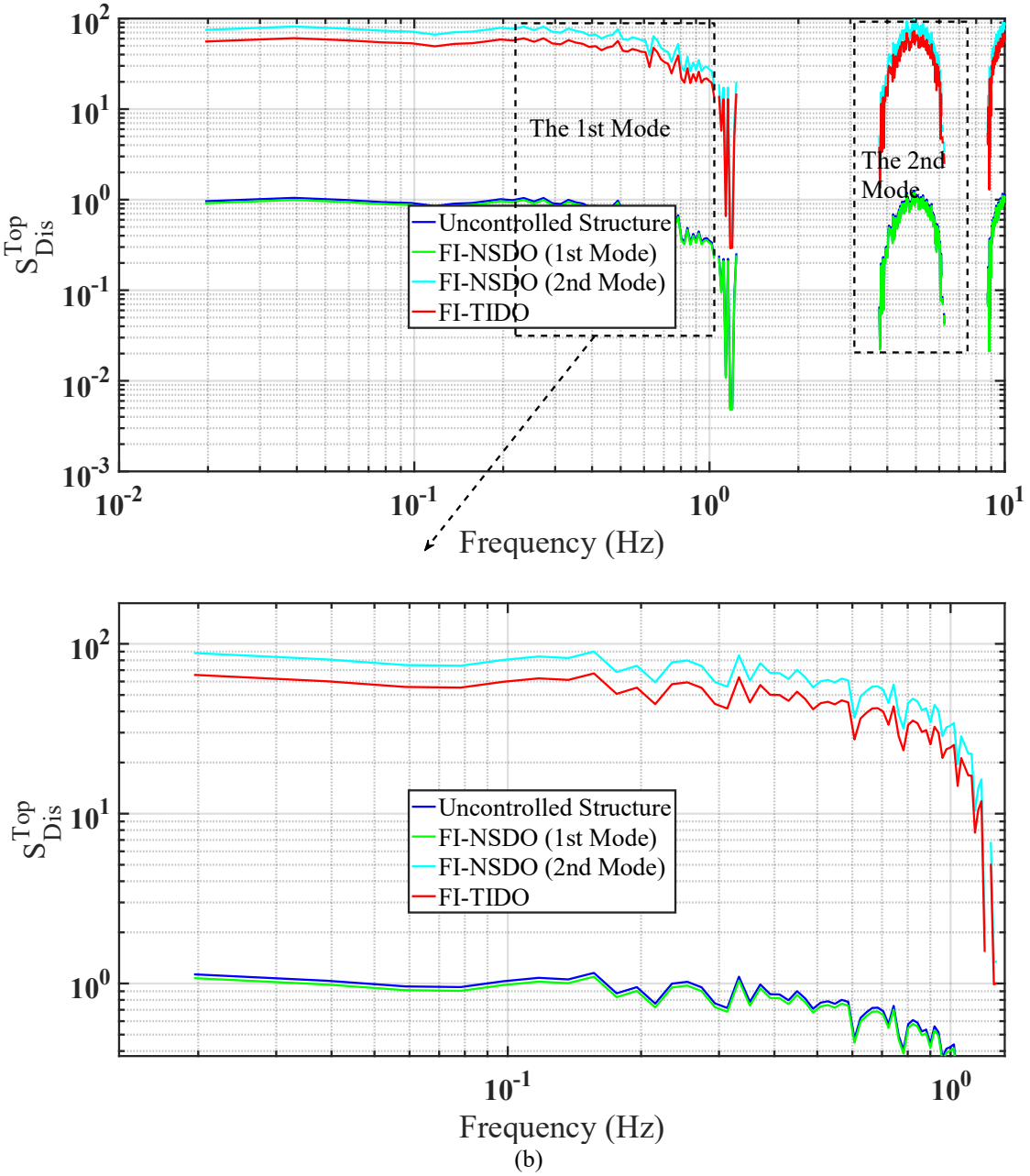
370 **Table 4** Optimally designed TIDO and FI-TIDO for seismic response.

Responses	TIDO (1st mode)	TIDO (2nd mode)	FI-TIDO
Top acceleration	1.345	0.7285	0.625
Top drift	0.985	1.425	0.708

371



(a)



(b)

372 **Fig. 11** Tall structure with FI-NSDO and FI-TIDO under seismic load for PSD curve response of: (a) Top
373 acceleration response; and (b) Top displacement response.

374 **4.3 Analysis of Time Domain**

375 The classical complex stiffness model is used to describe the frequency-independent characteristic as an FID, also
376 known as the noncausal model as a complex stiffness model (Inaudi and Kelly 1995). In time-domain analysis, both
377 stable and unstable poles occur simultaneously. Hence, to solve this issue, researchers use a complex stiffness model
378 such as the Maxwell-Wiechert model (Muscolino et al. 2005). However, the frequency domain is not highlighted in
379 some studies. Rather than, the researchers preferred time domain analysis, which results in simplifications of the non-

causality of the complex stiffness model. The method reported by Deastra et al. (Cao and Li 2019; Deastra et al. 2020) for the MDOF system under nonstationary excitation is adopted in this study.

Hilbert(Inaudi and Kelly 1995) suggested seismic response and excitation in time domain analysis for investigating complex signal forms by edifying the real and imaginary elements in time reversal technique, as follows:

$$y_a(t) = y(t) + iH[y(t)] \tag{35}$$

$$\ddot{x}_a(t) = \ddot{x}_g(t) + iH\left[\ddot{x}_g(t)\right] \tag{36}$$

where Hilbert transform is expressed as $H[\bullet]$. The boundary condition is satisfied by analytical signals of $y_a(-\infty) = y_a(\infty) = 0 \& \ddot{x}_a(-\infty) = \ddot{x}_a(\infty) = 0$.

Later, Eq. (26) is revised as

$$\dot{Y}_a = A_S Y_a + B_S \ddot{x}_a \tag{37.a}$$

$$P_a = C_S Y_a + D_S \ddot{x}_a \tag{37.b}$$

where a tall structure with the FI-TIDO system contains physical information represented as a system matrix as A_S. As mentioned earlier, complex equations cannot be solved directly by continuous integration since the noncausal model is used. Hence, A_S, as a pair of both stable and unstable roots of eigenvalue, are used. Inaudi and Makris (Inaudi and Makris 1996) suggested the backward integration technique by revealing time variables for solving unstable parts. The coordinates of stable and unstable are $p_a(t) \& q_a(t)$, expressed as:

$$Y_a(t) = \psi \begin{bmatrix} p_a(t) \\ q_a(t) \end{bmatrix} \tag{38}$$

where the eigenvector matrix of A_S is expressed as ψ, $p_a = p + jH[p]$ & $q_a = q + jH[q]$. In terms of the unstable coordinate, $q_a(t)$ expressed as inverse time $(\tau = -t)$ that results:

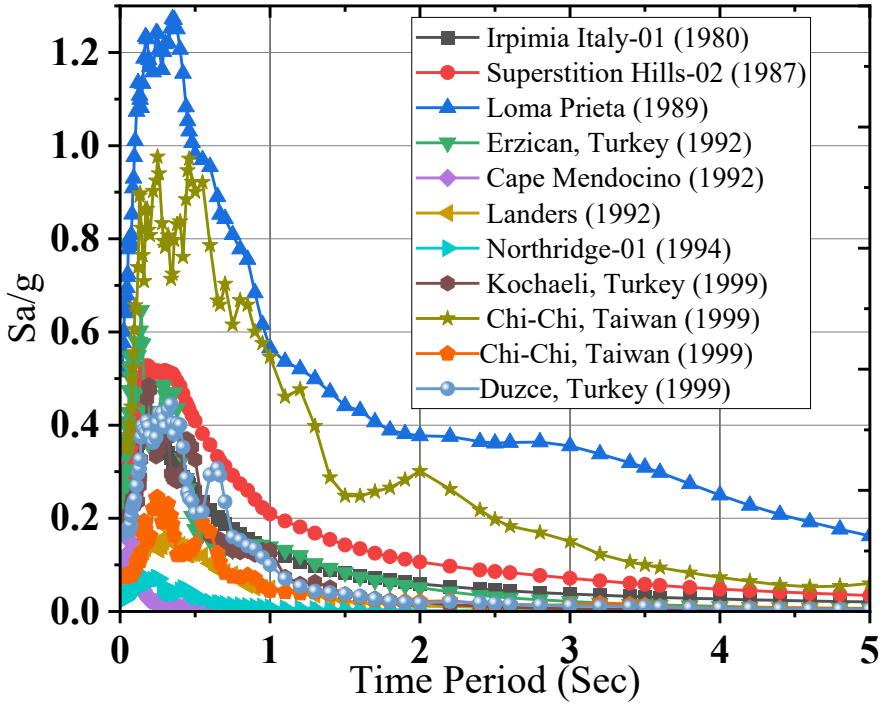
$$\tilde{q}(\tau) = q(t) \tag{39}$$

$$\tilde{q}'(\tau) = -\dot{q}(t) \tag{40}$$

where the derivate of the reverse of time (τ) is expressed as $\left[\ \ \right]'$. Eq. (35) is also modified as:

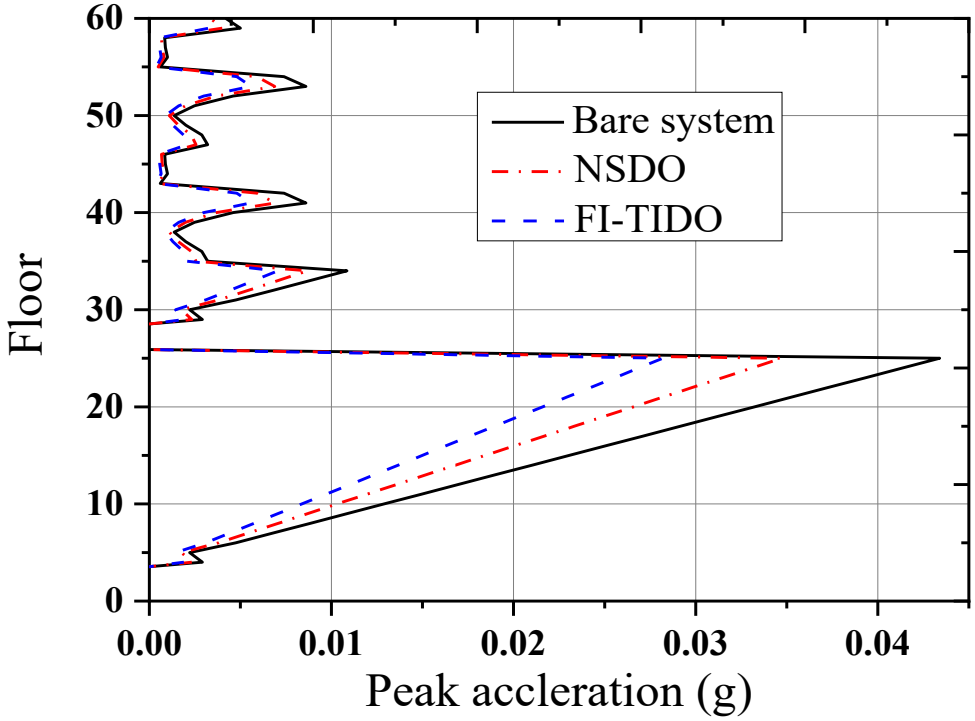
$$\begin{bmatrix} \dot{p}_a(t) \\ -\tilde{q}_a'(\tau) \end{bmatrix} = \tilde{A} \begin{bmatrix} p_a(t) \\ \tilde{q}_a(t) \end{bmatrix} + \tilde{B} \begin{bmatrix} \ddot{x}_a(t) \\ \ddot{x}_a'(\tau) \end{bmatrix} \tag{41}$$

Table 5 presents the ground motions considered in the present study. All selected ground motions are classified as near-field due to their characteristic high-frequency content and long-period pulses, as well as their diverse frequency components. Fig. 12 displays the peak pseudo-acceleration spectrum for the selected ground motions. Fig. 13 illustrates the reduction in peak acceleration and interstory drift of the tall structure subjected to the Chi-Chi earthquake, using NSDO and FI-TIDO control devices. The maximum peak acceleration at the 25th story is reduced from 0.045 g to 0.035 g and 0.028 g with the application of NSDO and FI-TIDO, respectively. Additionally, the minimum interstory drift at the 45th story is reduced from 0.1 to 0.008 when using TIDO in the first and second modes, and to 0.064 when using FI-TIDO.

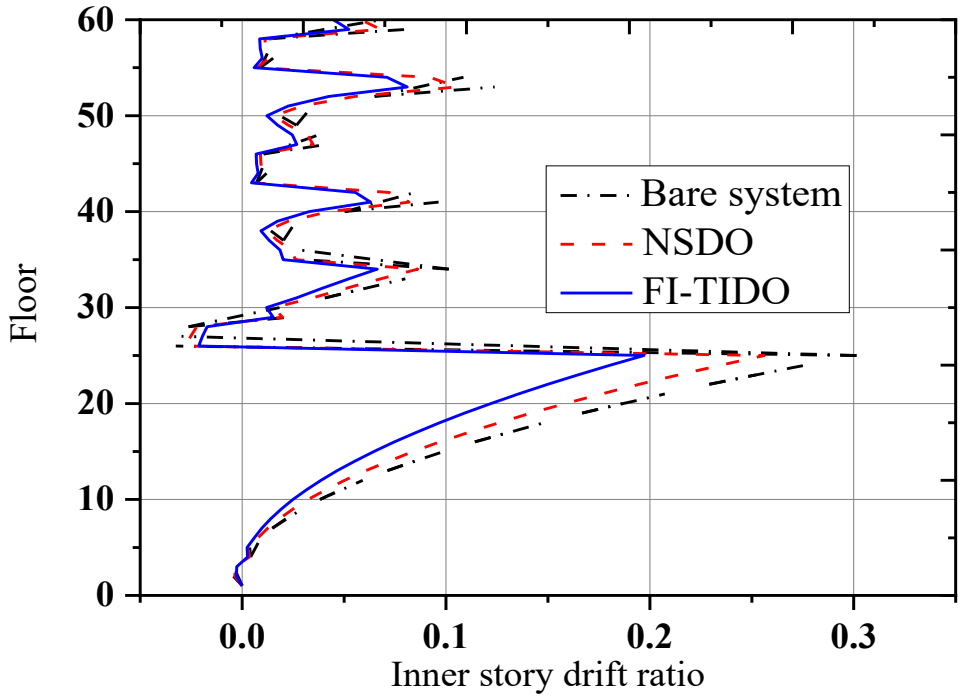


403

404 **Fig. 12** Eleven selected near fault response spectra of ground motion of 5% damping ratio.

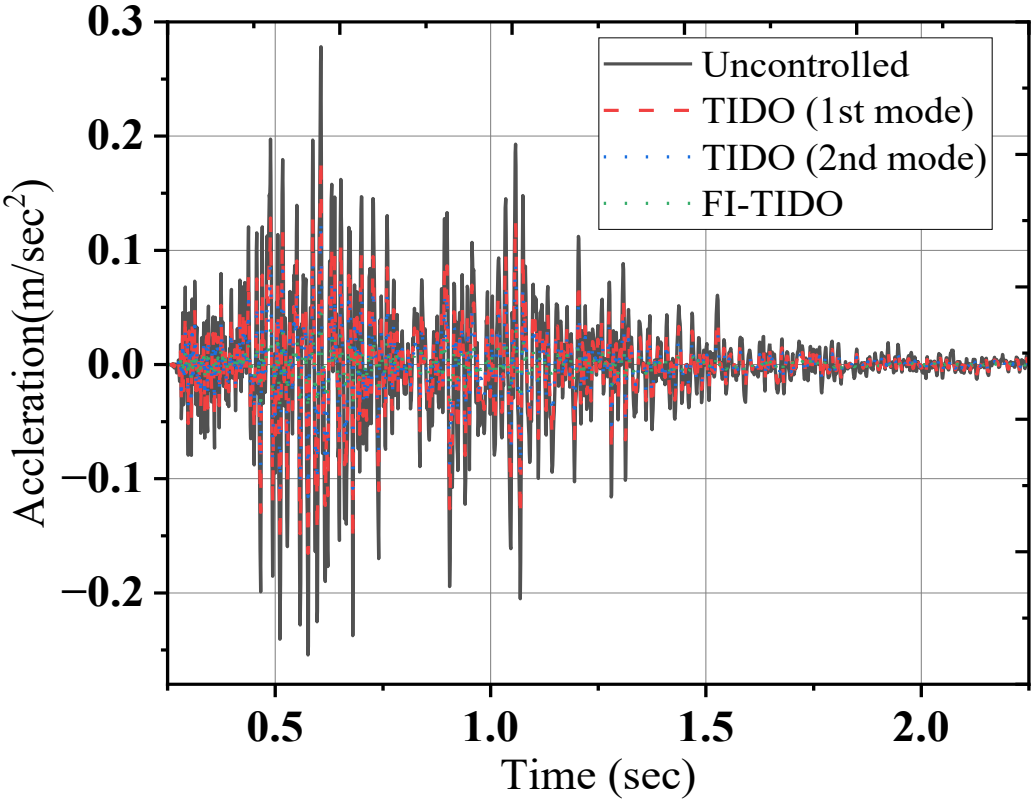


(a)

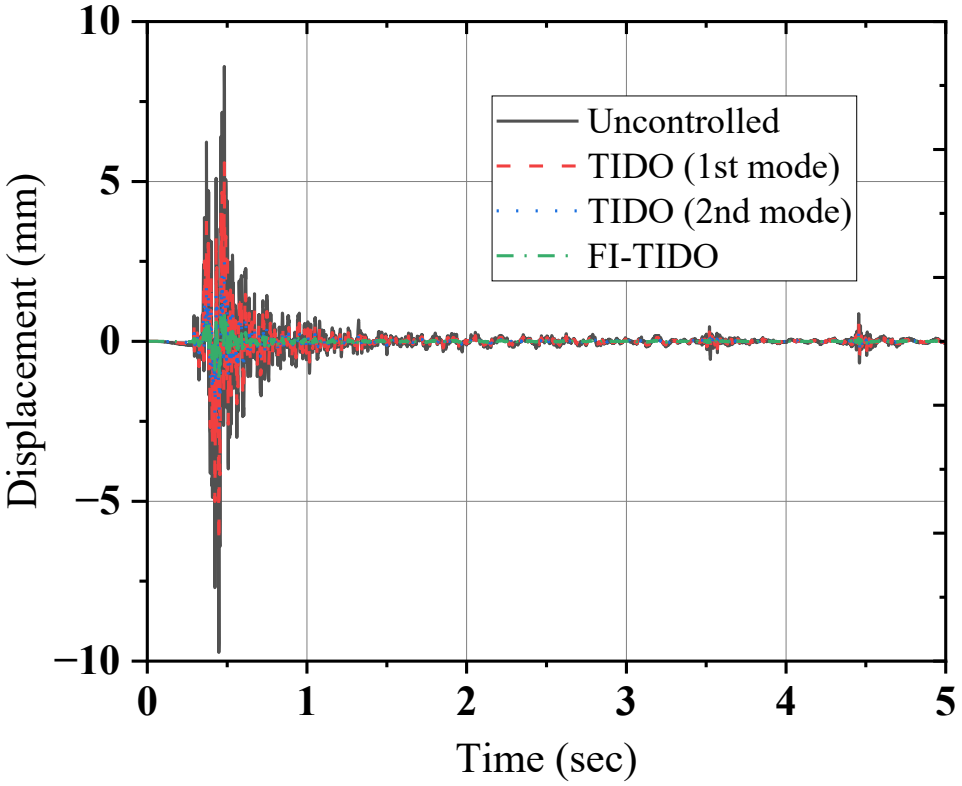


(b)

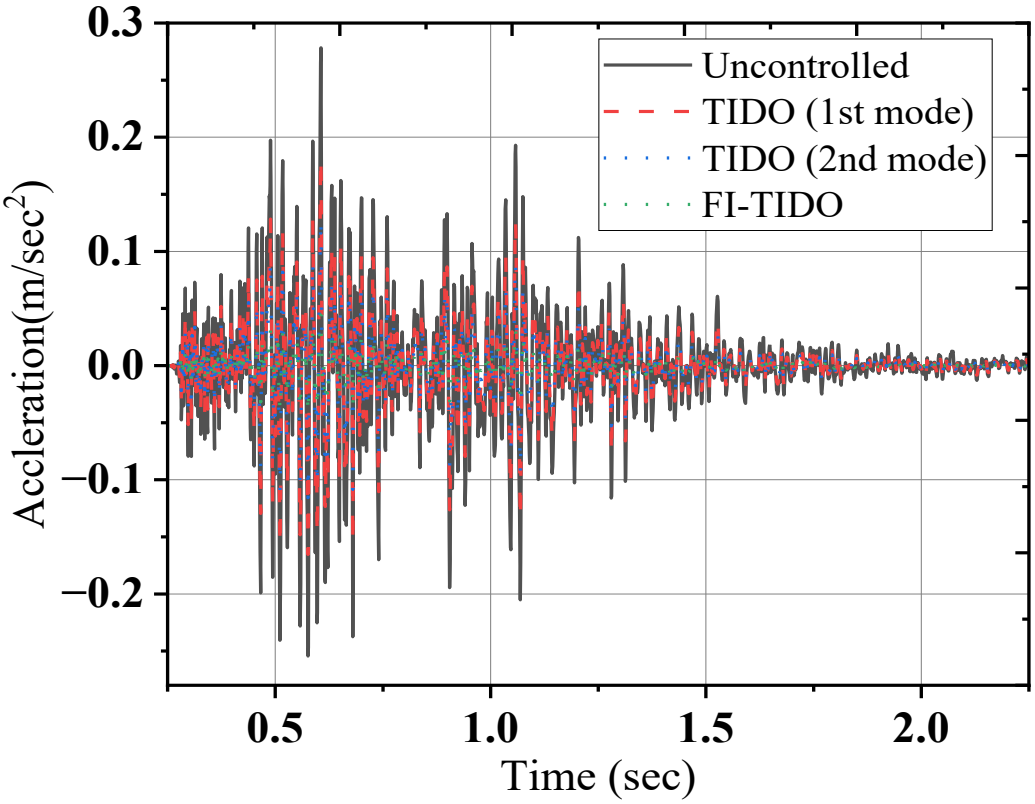
405 **Fig. 13** Tall structure under the Chi-Chi earthquake response envelops: (a) Acceleration; and (b) Drift ratio.



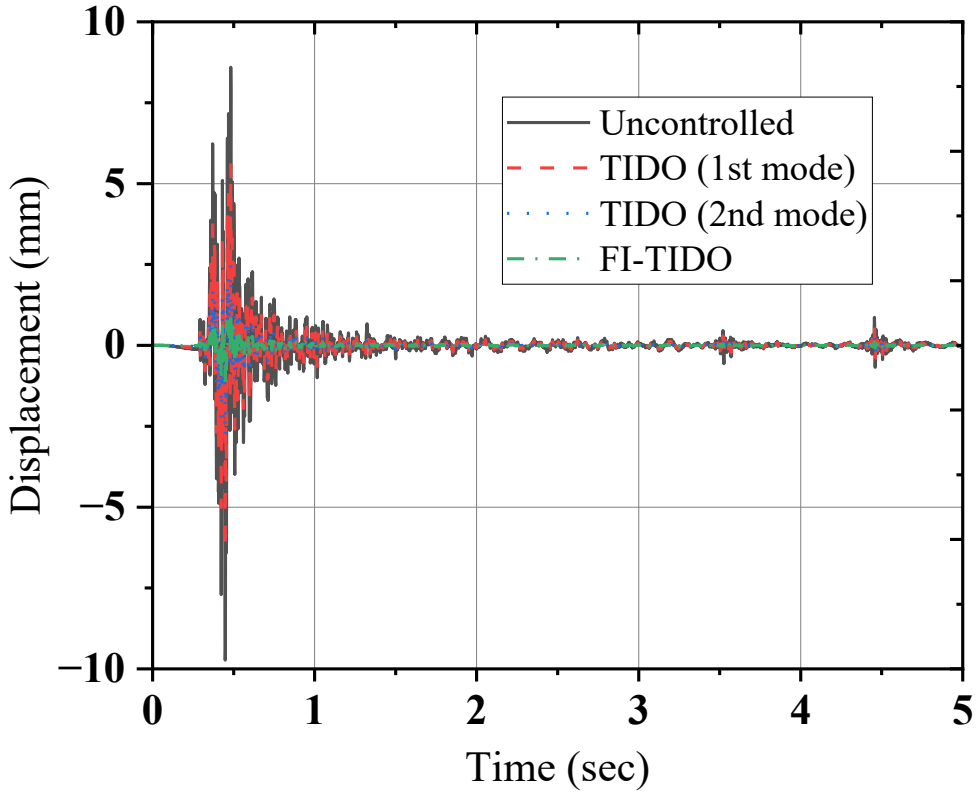
(a)


Uncontrolled
TIDO (1st mode)
TIDO (2nd mode)
FI-TIDO
Displacement (mm)
Time (sec)
10
5
0
−5
−10
0
1
2
3
4
5

(b)


Uncontrolled
TIDO (1st mode)
TIDO (2nd mode)
FI-TIDO
Accleration(m/sec²)
Time (sec)
0.3
0.2
0.1
0.0
−0.1
−0.2
0.5
1.0
1.5
2.0

(a)



(b)

406 **Fig. 14** Tall structure seismic response of time histories under the Duzce, Turkey (1999): (a) Top story acceleration;
407 and (b) Top story displacement.

408

409 **Table 5** Ground motion of the present study (Peer ground motion website). (Near Fault)

Earthquake	Year	M_w	Recording station	$V_{s,30}$ (m/sec)	Component	E_s (km)	PGA (g)
Irpinia, Italy-01	1980	6.9	Sturno	1000	MUL009	30.4	0.31
Superstition Hills-02	1987	6.5	Parachute Test Site	349	SUPERST	16.0	0.42
Loma Prieta	1989	6.9	LOMAP	371	HEC000	27.2	0.38
Erzican, Turkey	1992	6.7	Erzincan 11	275	ERZIKAN	9.00	0.49
Cape Mendocino	1992	7.0	CAPEMEND	713	NIS090	4.5	0.63
Landers	1992	7.3	Lucerne	685	LANDERS	44.0	0.79
Northridge-01	1994	6.7	Rinaldi Receiving Sta	282	NORTHR	10.9	0.87
Kocaeli, Turkey	1999	7.5	Izmit	811	KOCAELI	5.3	0.22
Chi-Chi, Taiwan	1999	7.6	TCU065	306	CHICHI	26.7	0.82
Chi-Chi, Taiwan	1999	7.6	TCU102	714	CHICHI	45.6	0.29
Duzce, Turkey	1999	7.1	Duzce	276	DUZCE	1.6	0.52

5.0 DYNAMIC PERFORMANCE OF THE PROPOSED SYSTEMS UNDER CROSSWIND EXCITATION

The power law, considered for the investigation of wind velocity profile within the atmospheric boundary layer, is expressed as:

$$U(z) = U_b \left(\frac{z}{b}\right)^a \tag{42}$$

where power law exponent component is a; wind basic height is b; corresponding wind velocity is U_b; and total height is z.

Crosswind excitation is complex because it contains vortex shedding, wind turbulence, and vortex shedding at the edge of tall structures compared to a long wind load. The crossing wind directions are critical in evaluating the dynamic performance of tall structures subjected to crosswind. Hence, the crosswind direction is considered in the present study. The tall structure having an aspect ratio greater than 3 consists of a crosswind response compared to a long wind response, as investigated by Linag et al. (Liang et al. 2002).

In the present study, data is obtained from the wind tunnel investigation by considering wind turbulence, vortex shedding, and the spatial correlation proposed by Liang et al. (Liang et al. 2002). For a tall structure, the power spectra formulae of the crosswind response of a rectangular plan are given as follows:

$$\frac{nS_F(n)}{\sigma^2} = A\frac{H(C_1)\bar{n}^2}{(1-\bar{n}^2)^2 + C_1\bar{n}^2} + (1-A)\frac{C_2^{0.50}\bar{n}^3}{[(1-\bar{n}^2)^2 + C_1\bar{n}^3]} \tag{43}$$

Other parameters are expressed as

$$H(C_1) = 0.179C_1 + 0.65\sqrt{C_1} \tag{44}$$

$$\left\{\begin{array}{c} C_1 = \dfrac{\left[0.47\left(\dfrac{D}{B}\right)^{2.8} - 0.52\left(\dfrac{D}{B}\right)^{\frac{1}{4}} + 0.24\right]}{\left(\dfrac{H}{\sqrt{S}}\right)} \\ C_2 = 2 \end{array}\right\} \tag{45}$$

$$A = \left\{\begin{array}{c} \left(\dfrac{H}{\sqrt{S}}\right)\left[-0.6\left(\dfrac{D}{B}\right)^2 + 0.29\left(\dfrac{D}{B}\right) - 0.06\right] + \left[9.84\left(\dfrac{D}{B}\right)^2 - 5.86\left(\dfrac{D}{B}\right) + 1.25\right], \dfrac{1}{4} \le \dfrac{D}{B} < \dfrac{1}{2} \\ \left(\dfrac{H}{\sqrt{S}}\right)\left[-0.118\left(\dfrac{D}{B}\right)^2 + 0.358\left(\dfrac{D}{B}\right) - 0.214\right] + \left[0.066\left(\dfrac{D}{B}\right)^2 - 0.26\left(\dfrac{D}{B}\right) + 0.894\right], \dfrac{1}{2} \le \dfrac{D}{B} < 3 \end{array}\right\} \tag{46}$$

where depth and width of the structural form are D and B, respectively; cross-section is S; force of spectrum is $S_F(n)$; frequency is n; frequency ratio is $\bar{n} = n/n_s$; and vortex shedding frequency is n_s. The experimental results obtained from the Strouhal number S_t are given below:

$$S_t = \begin{array}{c} 0.094, \dfrac{1}{4} \le \dfrac{D}{B} \le \dfrac{1}{2} \\ 0.002\left(\dfrac{D}{B}\right)^2 - 0.23\left(\dfrac{D}{B}\right) + 0.105, \dfrac{1}{2} \le \dfrac{D}{B} \le 4 \end{array} \tag{47}$$

The solution to the above expressions can be found in (Wang et al. 2022b).

Fig. 15 illustrates the amplification factor (AF) as a function of column stiffness for the FI-NSDO and FI-TIDO control devices, considering different inertance and frequency ratios. As the column stiffness increases, the corresponding AF

decreases for a 45-story tall structure. The damped outrigger system performs more effectively with higher inertance and frequency ratios.

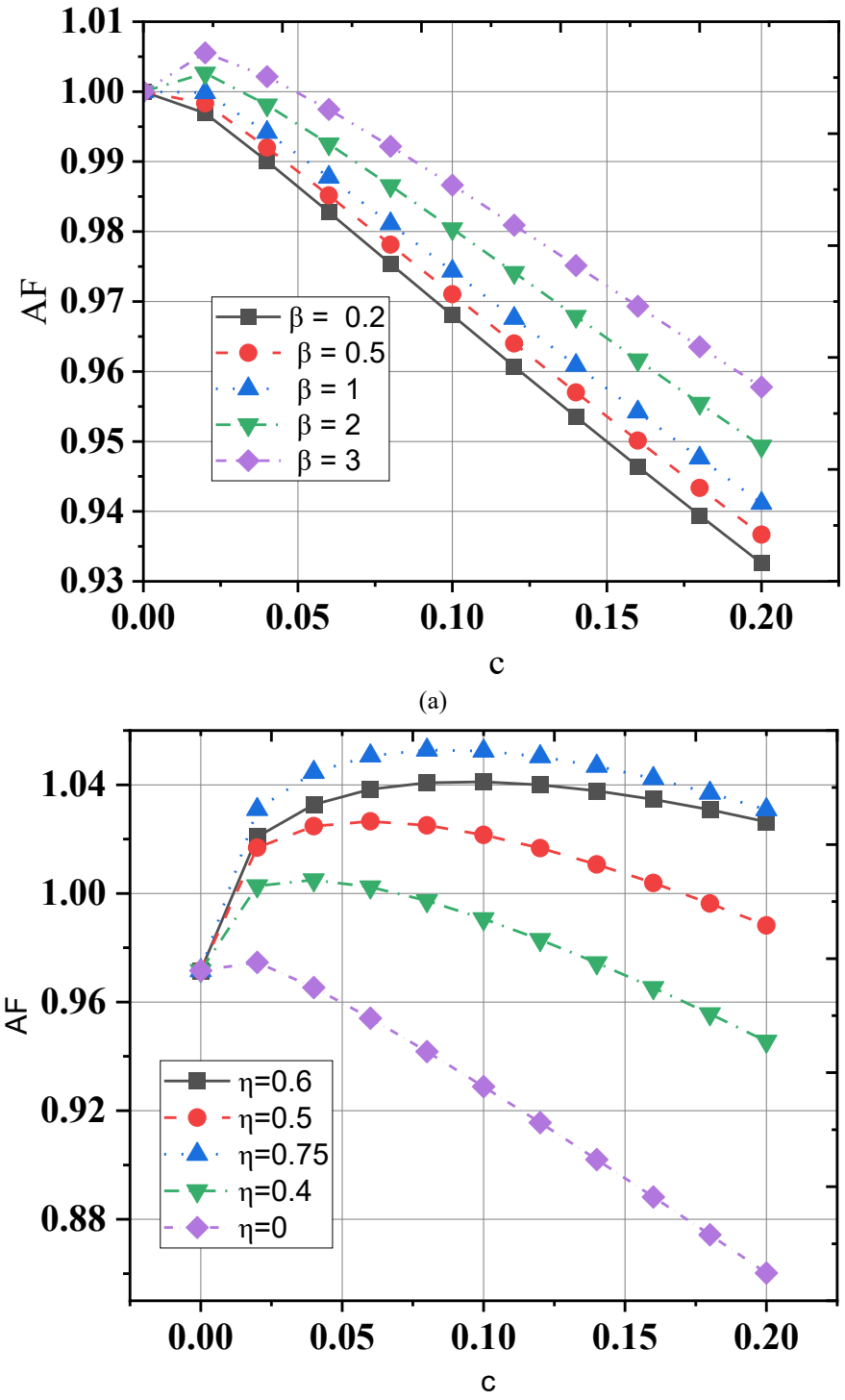
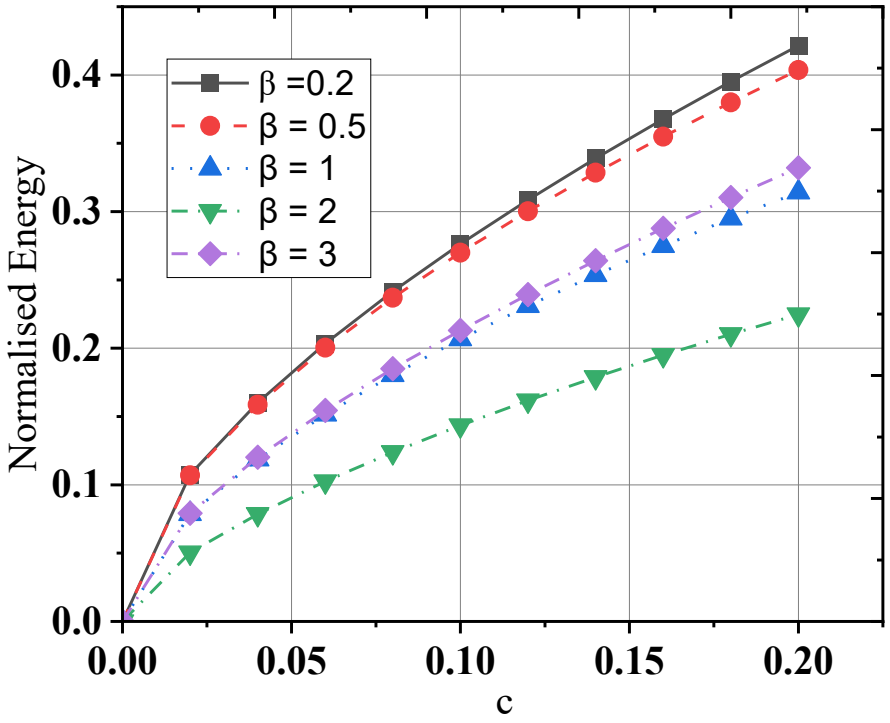
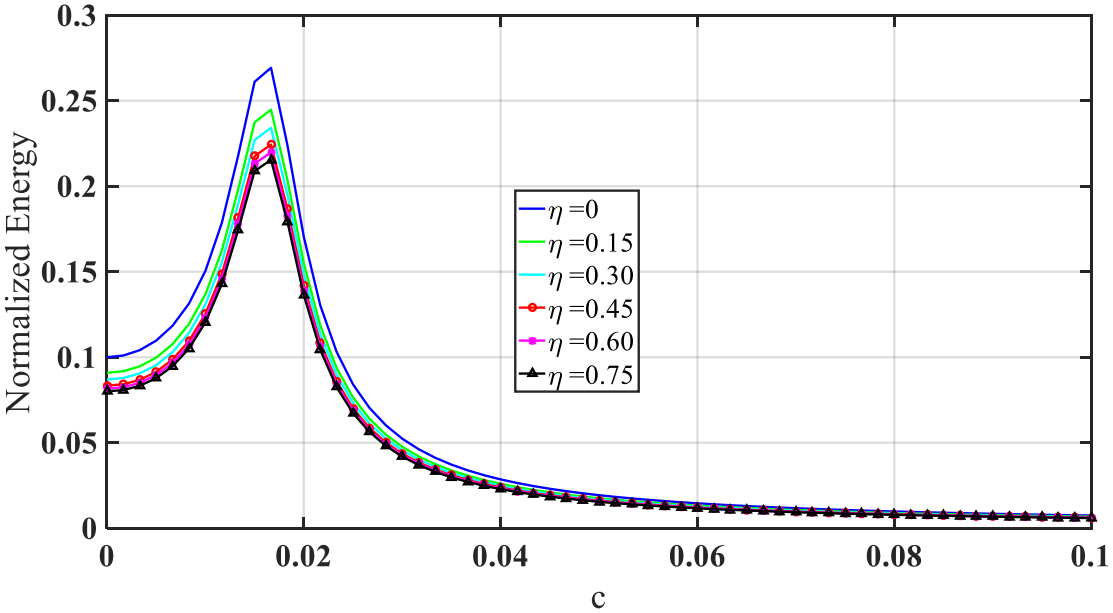


Fig. 15 Damping amplification factor of (a) NSDO and (b) FI-TIDO placed at 45 story for tall structure under crosswind excitation.

Fig. 16 presents the normalized energy dissipation for various column inertance and frequency ratios, and compares the dynamic performance of different control devices. Column stiffness plays a critical role in the structural response under novel wind excitations.

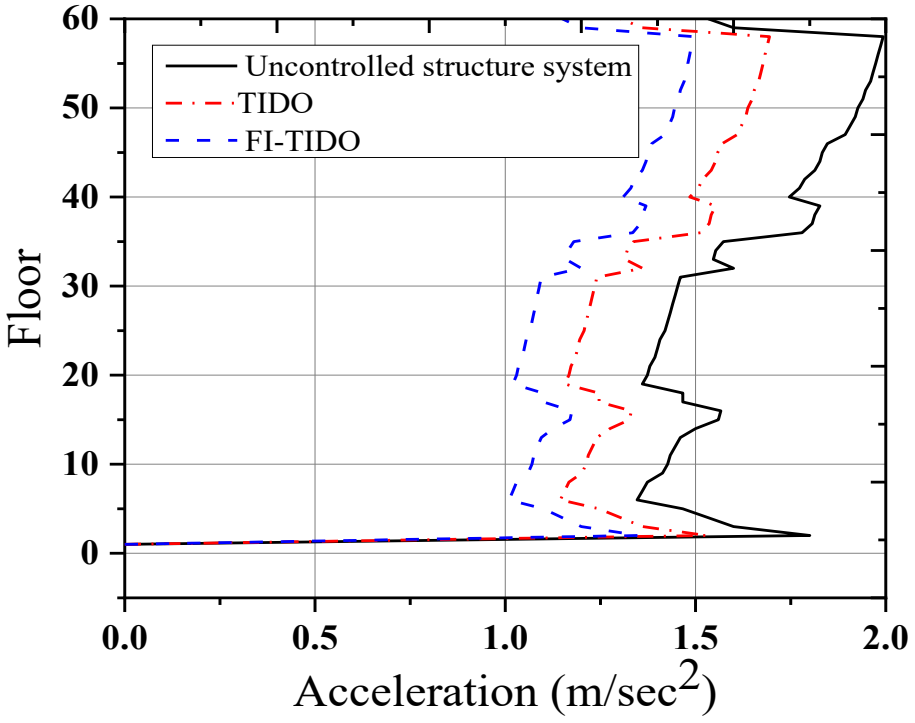


(a)

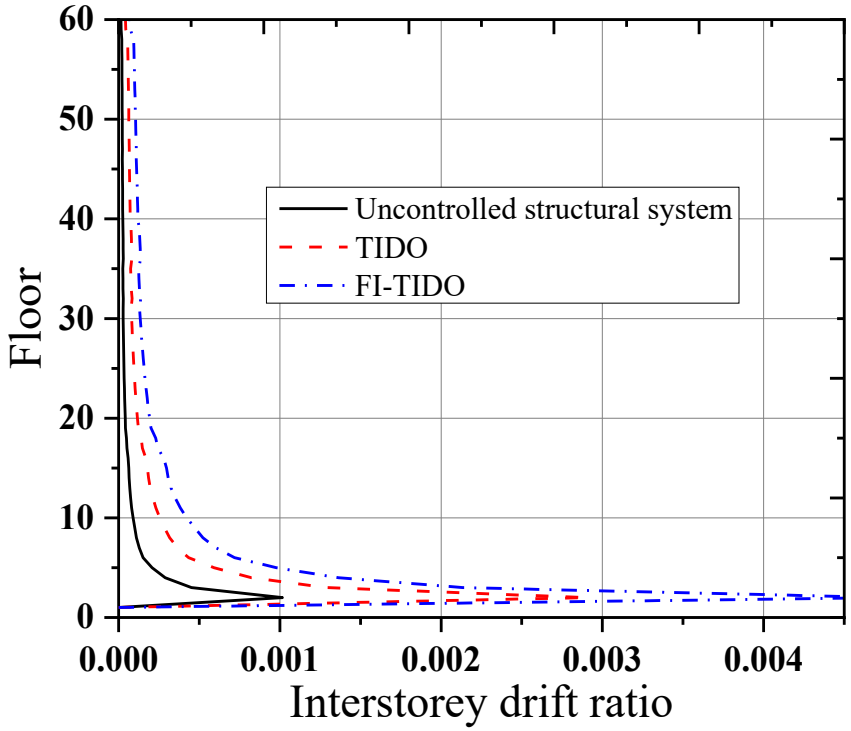


(b)

Fig. 16 Normalized energy dissipations of (a) NSDO and (b) FI-TIDO placed at 45 story for tall structure under crosswind excitation.



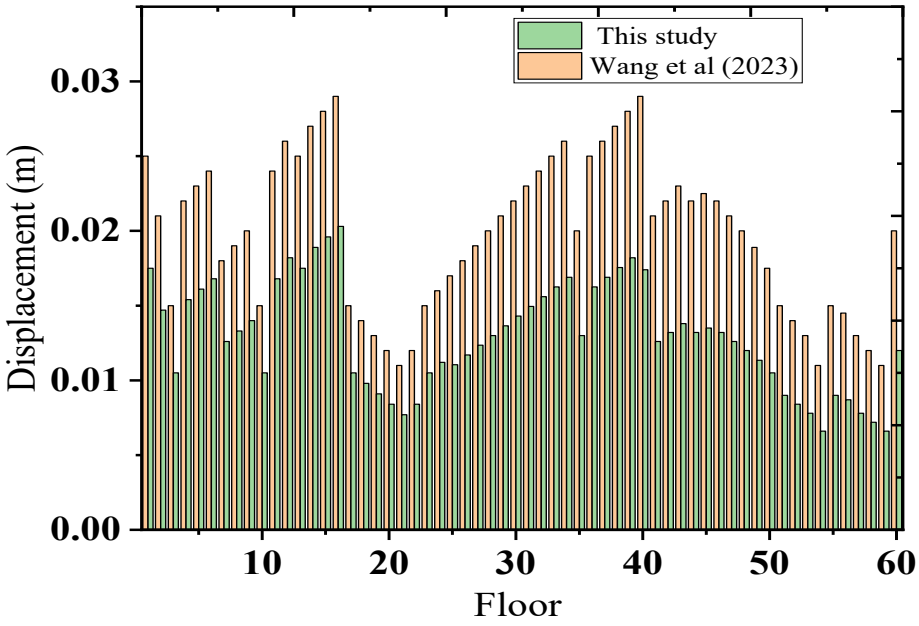
(a)



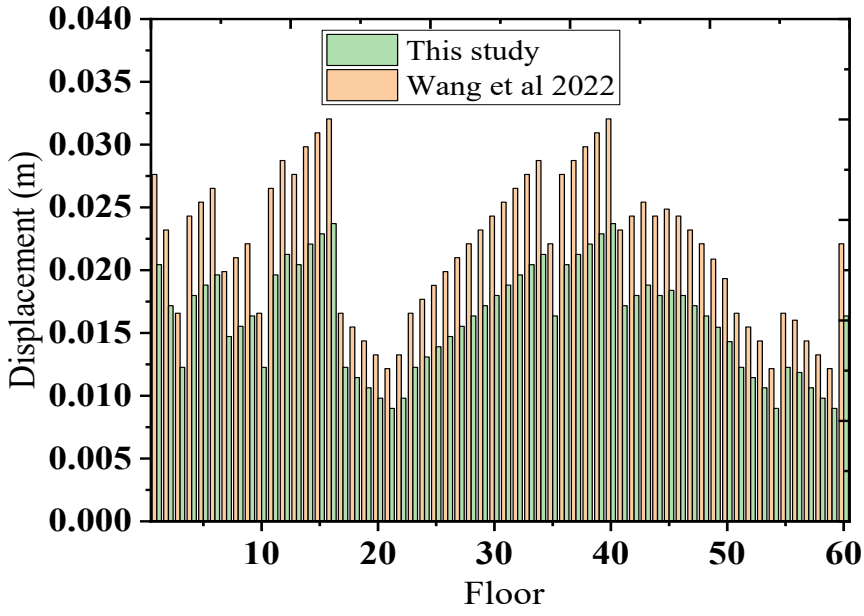
(b)

Fig. 17 A tall structure with several outrigger systems under wind action in the crosswind direction: (a) Acceleration of the structural system with the RMS value; and (b) Interstory drift ratio of the structural system with RMS value.

Fig. 17 shows the reduction in acceleration and interstory drift ratio of the tall structure under crosswind excitations. The FI-TIDO control device results in a greater reduction in the maximum response compared to TIDO. The improved crosswind performance originates from the ability of the frequency-independent damping mechanism to maintain nearly constant energy dissipation even when the vortex shedding frequency varies around the structural natural frequency. Unlike conventional tuned systems, the proposed FI-TIDO therefore remains effective under broadband wind excitation without requiring precise frequency tuning.



(a)



(b)

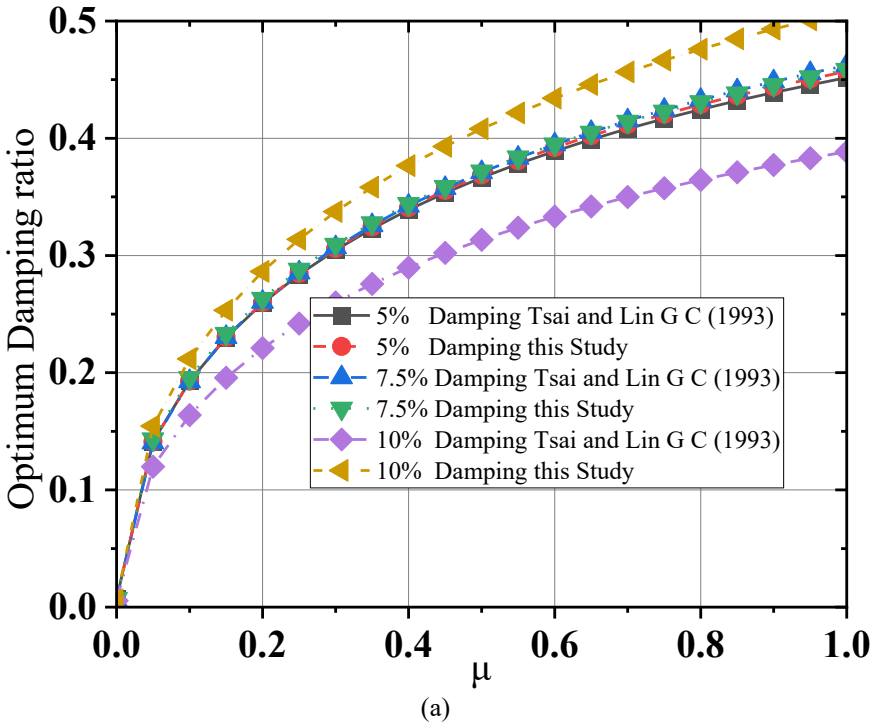
Fig. 18 Comparisons of the response of tall structure in the present study and previous researchers: (a) Under crosswind excitations; and (b) Under seismic excitations.

6.0 COMPARATIVE ANALYSIS WITH PREVIOUSLY PUBLISHED MODELS

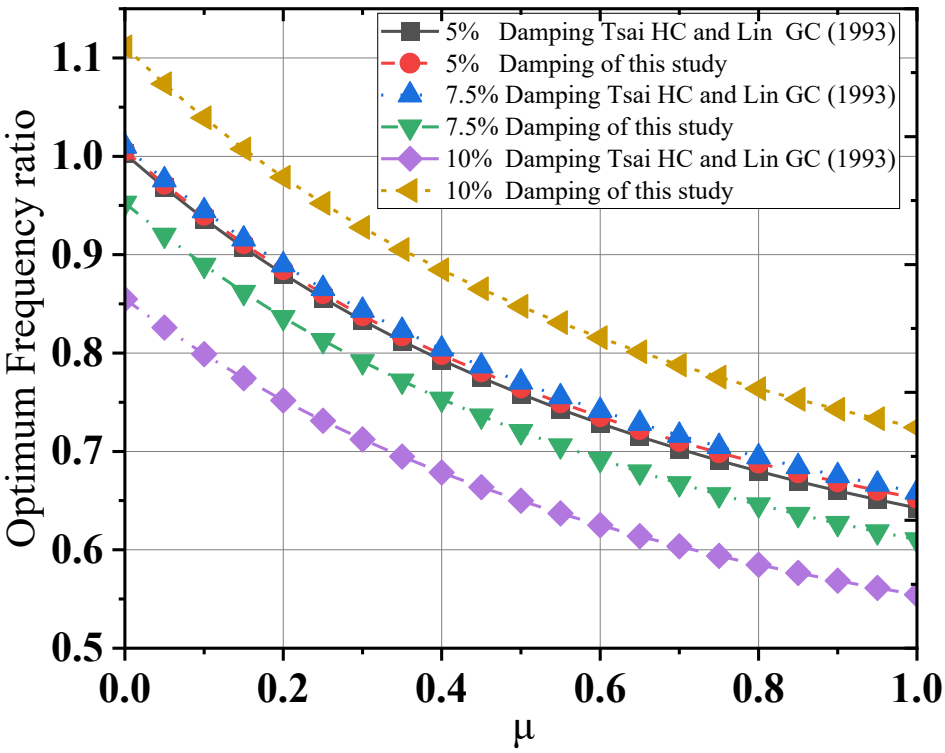
Fig. 18 (a) depicts the response of a tall structure under seismic excitation determined by the Newmark beta method. The displacement of the tall structure response is compared with the previous research by Wang et al. (Wang et al. 2023). The response is controlled by 35% higher than that of the present study. In addition, the displacement of tall structures under crosswind excitation is compared with previous research by Wang et al. (Wang et al. 2022c). The comparison reveals that the FI-TIDO plays a crucial role in mitigating dynamic responses under both seismic and wind loads. Unlike conventional dampers, which are typically tuned to a specific frequency, the FI-TIDO exhibits frequency-independent damping behaviour, allowing it to effectively suppress multimodal vibrations across a broader frequency range.

7.0 NUMERICAL VALIDATION

This study investigated the response of a single-degree-of-freedom (SDOF) system equipped with a TIDO (TID) damper under seismic loading using the Wilson theta method. The results of the optimal parameter ratio for the TID damper are found to agree with those reported by Tsai and Lin (Tsai and Lin 1993), as shown in Fig. 19. Additionally, the results of the optimum parameter ratio for the TMDI damper are found to agree with those reported by Su et al. (Su et al. 2022), as shown in Fig. 20. The optimum damping ratio and optimum frequency ratio for the SDOF system with TMDI are to be with those reported by Tigli (Tigli 2012) and Barredo et al., (Barredo et al. 2018), respectively, as shown in Table 6.

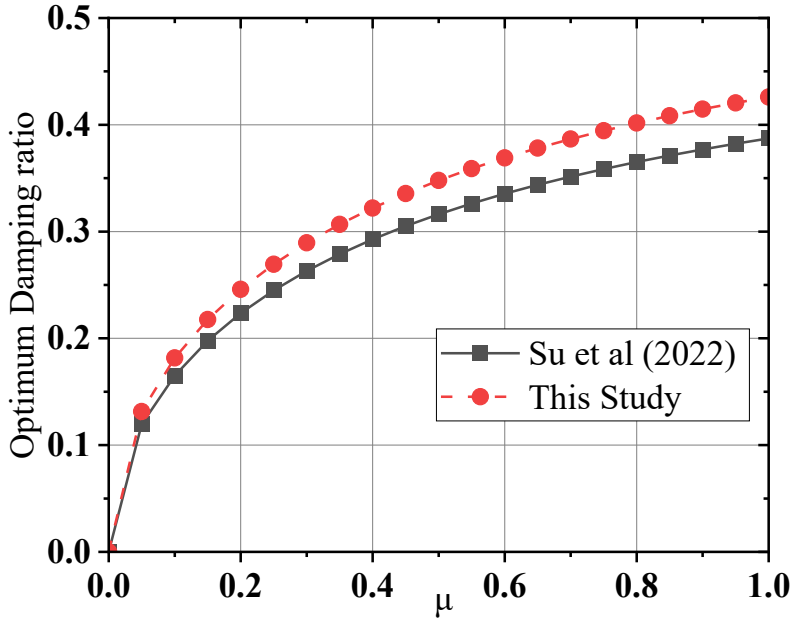


(a)

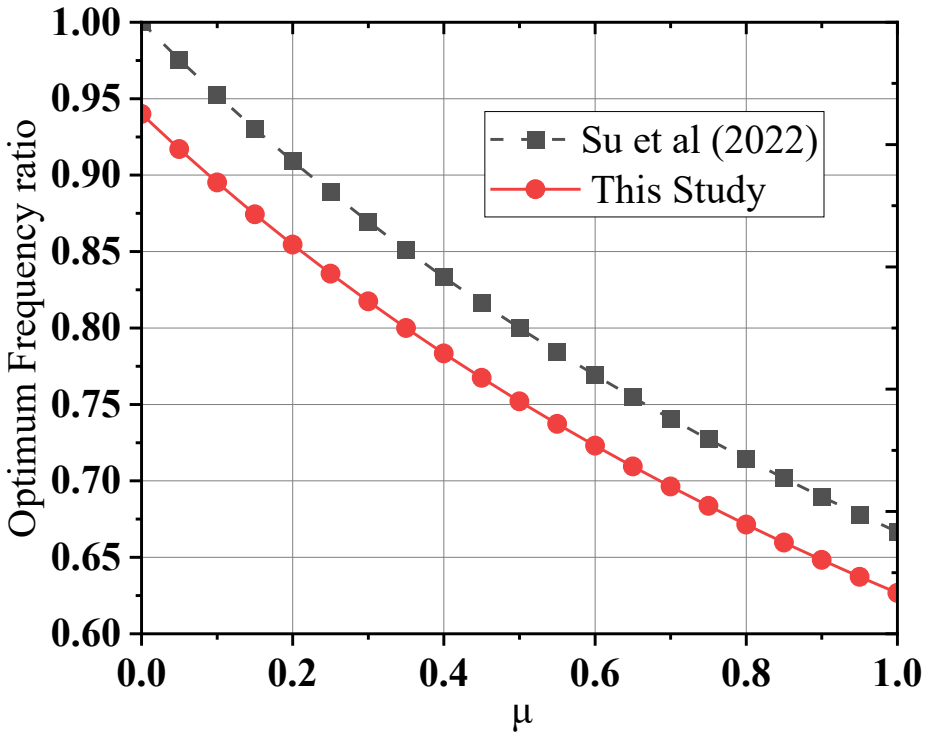


(b)

468 **Fig. 19** Comparison of optimum parameters of the present study and previous researchers (TMD).



(a)



(b)

Fig. 20 Comparison of optimum parameters of the present study and previous researchers (TMDI and H_∞ optimization).

Table 6 Comparison of optimum frequency ratio and optimum damping ratio with respect to inertance ratio of TMDI of present study and previous research investigation.

μ	Optimum frequency ratio				Optimum damping ratio			
	Tigli (Tigli 2012)	Hartog (Den Hartog 1947)	Barredo et al. (Barredo et al. 2018)	This study	Tigli (Tigli 2012)	Hartog (Den Hartog 1947)	Barredo et al. (Barredo et al. 2018)	This study
0.05	0.0000	0.0000	1.0000	0.0000	0.9500	1.0000	1.0000	0.7800
0.10	0.1572	0.1098	1.0247	0.1186	0.8830	0.9759	1.0247	0.7993
0.15	0.2211	0.1525	1.0488	0.1647	0.8234	0.9535	1.0488	0.8181
0.20	0.2694	0.1837	1.0724	0.1984	0.7703	0.9325	1.0724	0.8365
0.25	0.3096	0.2087	1.0954	0.2254	0.7227	0.9129	1.0954	0.8544
0.30	0.3446	0.2297	1.1180	0.2481	0.6798	0.8944	1.1180	0.8721
0.35	0.3760	0.2479	1.1402	0.2677	0.6409	0.8771	1.1402	0.8893
0.40	0.4045	0.2639	1.1619	0.2850	0.6057	0.8607	1.1619	0.9063
0.45	0.4309	0.2782	1.1832	0.3004	0.5735	0.8452	1.1832	0.9229
0.50	0.4556	0.2911	1.2042	0.3143	0.5441	0.8305	1.2042	0.9392
0.55	0.4787	0.3028	1.2247	0.3270	0.5171	0.8165	1.2247	0.9553
0.60	0.5006	0.3135	1.2450	0.3386	0.4923	0.8032	1.2450	0.9711
0.65	0.5214	0.3234	1.2649	0.3492	0.4694	0.7906	1.2649	0.9866
0.70	0.5413	0.3325	1.2845	0.3591	0.4482	0.7785	1.2845	1.0019
0.75	0.5603	0.3410	1.3038	0.3683	0.4286	0.7670	1.3038	1.0170
0.80	0.5786	0.3489	1.3229	0.3768	0.4104	0.7559	1.3229	1.0318
0.85	0.5963	0.3563	1.3416	0.3849	0.3934	0.7454	1.3416	1.0465
0.90	0.6133	0.3633	1.3601	0.3924	0.3775	0.7352	1.3601	1.0609
0.95	0.6298	0.3699	1.3784	0.3994	0.3627	0.7255	1.3784	1.0752
1.00	0.6459	0.3760	1.3964	0.4061	0.3489	0.7161	1.3964	1.0892
0.05	0.6614	0.3819	1.4142	0.4124	0.3359	0.7071	1.4142	1.1031

8.0 COMPARATIVE SUMMARY OF DAMPING STRATEGIES BASED ON DYNAMIC PERFORMANCE EVALUATION

Table 7 presents a comparative summary of various damping strategies - TMD, TMDI, CDO, NSDO, FI-NSDO, and the proposed FI-TIDO - based on their modal coverage, frequency-dependence, and effectiveness in reducing

structural response under seismic and crosswind excitations. The results clearly highlight the superior dynamic performance of FI-TIDO and FI-NSDO in multimodal damping, owing to their frequency-independent characteristics.

Table 7 Comparative Summary of Damping Strategies Based on Dynamic performance Evaluation.

Damping System	Frequency-Dependence	Modal Coverage	Energy Dissipation Mechanism	Key Limitations	Performance in Study
TMD (Tuned Mass Damper)	Yes	Primarily 1st mode	Resonance-based mass displacement	Ineffective in higher modes; limited for multi-hazard	Not evaluated numerically
TMDI (Tuned Mass Damper Inerter)	Yes	1st + Partial 2nd	Mass + inertance; enhanced control	Still frequency-tuned; not robust to broadband input	Not evaluated numerically
CDO (Conventional Damped Outrigger)	Yes	Partial multimodal	Viscous damping via outriggers	Limited by column stiffness and damping localization	Max $\xi_1 \approx 2.89\%$
NSDO (Negative Stiffness Damped Outrigger)	Partially	1st to 2nd mode	Energy redistribution via negative stiffness	Sensitive to tuning; not fully frequency-independent	Max $\xi_1 \approx 24.32\%$
FI-NSDO	No	Multimodal	Frequency-independent complex stiffness + negative stiffness	More complex implementation; requires fine-tuned parameters	High damping across modes
FI-TIDO	No	Fully multimodal	Inerter, negative stiffness, and FID hybrid	Design complexity; parameter identification	*Best performance: drift ↓ 32.5%, acc. ↓ 23.45%*

9.0 CONCLUSIONS

This study presented a comprehensive analytical framework for the development and evaluation of Frequency-Independent Tuned Inerter Damper Outrigger (FI-TIDO) and Frequency-Independent Negative Stiffness Damper Outrigger (FI-NSDO) systems for multimodal vibration control of tall buildings subjected to seismic and crosswind excitations. By integrating frequency-independent hysteretic damping with inerter and negative stiffness mechanisms into conventional outrigger systems, the proposed configurations overcome the inherent bandwidth limitations of conventional frequency-dependent passive control devices and provide enhanced vibration mitigation over a broad frequency range. The proposed analytical formulations were verified through comprehensive frequency-domain and nonlinear time-history analyses using a benchmark 60-story building.

Based on the analytical and numerical results, the following conclusions can be drawn:

1) The proposed frequency-independent outrigger systems substantially increased the equivalent modal damping of the benchmark building. A maximum first-mode damping ratio of 24.32% was achieved,

compared with 2.89% for the conventional damped outrigger system, demonstrating its effectiveness for multimodal vibration control.

2) Under eleven selected near-fault earthquake records, the FI-TIDO system reduced the average inter-story drift and floor acceleration by 32.5% and 23.45%, respectively, relative to the conventional TIDO and NSDO configurations, indicating improved seismic response mitigation.
3) The proposed system maintained effective vibration mitigation over a broad frequency range under crosswind excitation, providing improved displacement control, particularly under resonance conditions associated with vortex shedding. These characteristics contribute to enhanced structural serviceability and occupant comfort in slender tall buildings.
4) The incorporation of frequency-independent hysteretic damping enabled efficient energy dissipation over multiple vibration modes without requiring tuning to a single dominant structural frequency. Consequently, the proposed system offers an effective passive vibration control strategy for broadband dynamic hazards where higher-mode effects are significant.
5) Comparisons with published analytical and numerical studies showed good agreement in terms of dynamic characteristics and response trends, thereby supporting the accuracy of the proposed analytical formulations and their applicability for the analysis and design of advanced outrigger-based vibration control systems.

Overall, the proposed frequency-independent outrigger systems provide an analytical basis for improving the seismic and wind performance of tall buildings through broadband multimodal vibration control. The developed analytical framework offers a computationally efficient tool for the preliminary design, evaluation, and optimization of advanced outrigger systems and may facilitate the development of practical passive vibration control solutions for future high-rise structures.

The present study is limited to linear structural behaviour under unidirectional excitation and does not explicitly account for soil–structure interaction, material and geometric nonlinearities, torsional effects, structural pounding, or uncertainties associated with structural and loading parameters. Although the proposed analytical framework provides useful insights into the dynamic characteristics of frequency-independent outrigger systems, additional studies are required before practical implementation. Future work will focus on extending the proposed formulations to bidirectional and multi-hazard excitations, incorporating nonlinear structural behaviour and soil–structure interaction, investigating performance under uncertainty, and validating the proposed systems through experimental and hybrid numerical–experimental studies.

REFERENCES

Aly AM (2014) Proposed robust tuned mass damper for response mitigation in buildings exposed to multidirectional wind. The Structural Design of Tall and Special Buildings 23(9):664–691. https://doi.org/10.1002/tal.1068

Asai T, Chang C-M, Phillips BM, Spencer BF (2013) Real-time hybrid simulation of a smart outrigger damping system for high-rise buildings. Engineering Structures 57:177–188. https://doi.org/10.1016/j.engstruct.2013.09.016

Bae SH, Cho JR, Bae SR, Jeong WB (2014) A discrete convolutional Hilbert transform with the consistent imaginary initial conditions for the time-domain analysis of five-layered viscoelastic sandwich beam. Computer Methods in Applied Mechanics and Engineering 268:245–263. https://doi.org/10.1016/j.cma.2013.09.010

Banavalkar PV (1990) Structural systems to improve wind induced dynamic performance of high rise buildings. Journal of Wind Engineering and Industrial Aerodynamics 36:213–224. https://doi.org/10.1016/0167-6105(90)90306-W

Barredo E, Blanco A, Colín J, Penagos VM, Abúndez A, Vela LG, Meza V, Cruz RH, Mayén J (2018) Closed-form solutions for the optimal design of inerter-based dynamic vibration absorbers. International Journal of Mechanical Sciences 144:41–53. https://doi.org/10.1016/j.ijmecsci.2018.05.025

Cao L, Li C (2019) Tuned tandem mass dampers-inerters with broadband high effectiveness for structures under white noise base excitations. Structural Control and Health Monitoring 26(4):e2319. https://doi.org/10.1002/stc.2319

Chen Y, McFarland DM, Wang Z, Spencer BF, Bergman LA (2010) Analysis of Tall Buildings with Damped Outriggers. Journal of Structural Engineering 136(11):1435–1443. https://doi.org/10.1061/(ASCE)ST.1943-541X.0000247

Chowdhury S, Debbarma R (2026) Optimum inerter tuned liquid column dampers: Exact closed-form expressions. Earthq Eng Eng Vib 25(2):555–577. https://doi.org/10.1007/s11803-026-2392-2

Cimellaro GP, Domaneschi M, Warn G (2020) Three-Dimensional Base Isolation Using Vertical Negative Stiffness Devices. Journal of Earthquake Engineering 24(12):2004–2032. https://doi.org/10.1080/13632469.2018.1493004

Clough RW, Penzien J (1975) Dynamics of Structures. McGraw-Hill

Constantinou MC, Tsopelas P, Hammel W, Sigaher AN (2001) Toggle-Brace-Damper Seismic Energy Dissipation Systems. Journal of Structural Engineering 127(2):105–112. https://doi.org/10.1061/(ASCE)0733-9445(2001)127:2(105)

Dai J, Wang Y, Wei M, Zhang W, Zhu J, Jin H, Jiang C (2022) Dynamic characteristic analysis of the inerter-based piecewise vibration isolator under base excitation. Acta Mech 233(2):513–533. https://doi.org/10.1007/s00707-021-03115-0

Daniel Y, Lavan O (2014) Gradient based optimal seismic retrofitting of 3D irregular buildings using multiple tuned mass dampers. Computers & Structures 139:84–97. https://doi.org/10.1016/j.compstruc.2014.03.002

Das S, Tesfamariam S (2020) Optimization of SMA based damped outrigger structure under uncertainty. Engineering Structures 222:111074. https://doi.org/10.1016/j.engstruct.2020.111074

Deastra P, Wagg D, Sims N, Akbar M (2020) Tuned inerter dampers with linear hysteretic damping. Earthquake Engineering & Structural Dynamics 49(12):1216–1235. https://doi.org/10.1002/eqe.3287

Den Hartog J (1947) The Undamped and Damped Dynamic Vibration Absorbers. Mechanical Vibrations 3:112–113

Elias S, Matsagar V (2018) Wind response control of tall buildings with a tuned mass damper. Journal of Building Engineering 15:51–60. https://doi.org/10.1016/j.jobe.2017.11.005

Fujino Y, Hoang N (2008) Design Formulas for Damping of a Stay Cable with a Damper. Journal of Structural Engineering 134(2):269–278. https://doi.org/10.1061/(ASCE)0733-9445(2008)134:2(269)

565 Gu M, Su L, Quan Y, Huang J, Fu G (2022) Experimental study on wind-induced vibration and aerodynamic
566 mitigation measures of a building over 800 meters. Journal of Building Engineering 46:103681.
567 https://doi.org/10.1016/j.jobe.2021.103681

568 Huang S, Zhu K (2026) Machine learning-based Bayesian optimization of tuned inerter dampers for enhanced seismic
569 response control in high-rise base-isolated structures. Sci Rep 16(1):13216. https://doi.org/10.1038/s41598-
570 026-42732-4

571 Inaudi JA, Kelly JM (1995) Linear Hysteretic Damping and the Hilbert Transform. Journal of Engineering Mechanics
572 121(5):626–632. https://doi.org/10.1061/(ASCE)0733-9399(1995)121:5(626)

573 Inaudi JA, Makris N (1996) Time-Domain Analysis of Linear Hysteretic Damping. Earthquake Engineering &
574 Structural Dynamics 25(6):529–545. https://doi.org/10.1002/(SICI)1096-9845(199606)25:6%3C529::AID-
575 EQE549%3E3.0.CO;2-P

576 Javanbakht M, Cheng S, Ghrib F (2020) Multimode vibration control of stay cables using optimized negative stiffness
577 damper. Structural Control and Health Monitoring 27(4). https://doi.org/10.1002/stc.2503

578 John NE, Kamath K (2023) An investigation on optimal outrigger locations for hybrid outrigger system under wind
579 and earthquake excitation. Asian J Civ Eng 24(3):759–778. https://doi.org/10.1007/s42107-022-00528-7

580 Kamgar R, Gholami F, Zarif Sanayei HR, Heidarzadeh H (2020) Modified Tuned Liquid Dampers for Seismic
581 Protection of Buildings Considering Soil–Structure Interaction Effects. Iran J Sci Technol Trans Civ Eng
582 44(1):339–354. https://doi.org/10.1007/s40996-019-00302-x

583 Kaveh A, Fahimi Farzam M, Hojat Jalali H, Maroofiazar R (2020) Robust optimum design of a tuned mass damper
584 inerter. Acta Mech 231(9):3871–3896. https://doi.org/10.1007/s00707-020-02720-9

585 Kaveh A, Mohammadi S, Hosseini OK, Keyhani A, Kalatjari V (2015) Optimum parameters of tuned mass dampers
586 for seismic applications using charged system search. Iranian Journal of Science and Technology
587 Transactions of Civil Engineering 39(C1):21

588 Kawai H (1992) Vortex induced vibration of tall buildings. Journal of Wind Engineering and Industrial Aerodynamics
589 41(1–3):117–128. https://doi.org/10.1016/0167-6105(92)90399-U

590 Khatibinia M, Bijari S, Nezhad FSM, Gharehbaghi S (2025) Seismic Vulnerability Control of Steel Moment–Resisting
591 Frames Using Optimum Friction Tuned Mass Damper. Iran J Sci Technol Trans Civ Eng 49(1):165–182.
592 https://doi.org/10.1007/s40996-024-01453-2

593 Kiran KK, Al-Osta MA, Ahmad S (2023) Optimum design and performance of a base-isolated structure with tuned
594 mass negative stiffness inerter damper. Sci Rep 13(1):4980. https://doi.org/10.1038/s41598-023-31482-2

595 Kiran KK, Naveenkumar DT (2025a) Advanced Damping Strategies for High-Rise Structures: Multi-Modal Vibration
596 Mitigation Using Tuned Mass Inerter Dampers and Negative Stiffness Outriggers. Iran J Sci Technol Trans
597 Civ Eng. https://doi.org/10.1007/s40996-025-01904-4

598 Kiran KK, Naveenkumar DT (2024) An innovative hybrid methodology for vibration control of inerter-assisted sliding
599 isolation system under harmonic excitation. Asian J Civ Eng 25(5):3943–3960.
600 https://doi.org/10.1007/s42107-024-01022-y

601 Kiran KK, Naveenkumar DT (2025b) Dynamic Response Mitigation of Adjacent Structures Using Negative Stiffness
602 Amplifying Dampers Under Seismic and Cyclic Pulse Excitations. Iran J Sci Technol Trans Civ Eng.
603 https://doi.org/10.1007/s40996-025-01807-4

Kiran KK, Naveenkumar DT (2026) Nonlinear Dynamic Analysis and Closed-Form Modelling of Negative Stiffness Vibration Isolation Systems Under Bidirectional Excitation. Iran J Sci Technol Trans Mech Eng. https://doi.org/10.1007/s40997-026-00996-1

Kiran KK, Naveenkumar DT, Kumar AM (2025) Seismic vulnerability mitigation of base isolated structures equipped using a novel tuned mass dampers with H2 optimization. Asian J Civ Eng 26(3):1129–1142. https://doi.org/10.1007/s42107-024-01238-y

Kiran KK, Noroozinejad Farsangi E, Gharehbaghi V (2022) An innovative negative stiffness-inerter hybrid control device toward seismic-resilient structures. Innov Infrastruct Solut 7(5):310. https://doi.org/10.1007/s41062-022-00904-x

Kontoni D-PN, Farghaly AA (2023) Enhancing the earthquake resistance of RC and steel high-rise buildings by bracings, shear walls and TMDs considering SSI. Asian J Civ Eng 24(7):2595–2608. https://doi.org/10.1007/s42107-023-00666-6

Kontoni D-PN, Farghaly AA (2024a) Seismic control of T-shape in plan steel high-rise buildings with SSI effect using tuned mass dampers. Asian J Civ Eng 25(2):1725–1739. https://doi.org/10.1007/s42107-023-00873-1

Kontoni D-PN, Farghaly AA (2024b) Seismic control of vertically and horizontally irregular steel high-rise buildings by tuned mass dampers including SSI. Asian J Civ Eng 25(2):1995–2014. https://doi.org/10.1007/s42107-023-00890-0

Lamb S, Kwok KCS (2017) The fundamental human response to wind-induced building motion. Journal of Wind Engineering and Industrial Aerodynamics 165:79–85. https://doi.org/10.1016/j.jweia.2017.03.002

Li J, Duan L, Zhou Q, Su Q (2026) Intelligent hybrid optimization of tuned inerter dampers in base-isolated multi-storey structures under near-fault pulse-like ground motions. Sci Rep 16(1):10051. https://doi.org/10.1038/s41598-026-40831-w

Liang S, Liu S, Li QS, Zhang L, Gu M (2002) Mathematical model of acrosswind dynamic loads on rectangular tall buildings. Journal of Wind Engineering and Industrial Aerodynamics 90(12–15):1757–1770. https://doi.org/10.1016/S0167-6105(02)00285-4

Lin P-C, Takeuchi T, Matsui R (2018) Seismic performance evaluation of single damped-outrigger system incorporating buckling-restrained braces. Earthquake Engineering & Structural Dynamics. https://doi.org/10.1002/eqe.3072

Liu L, Tan P, Ma H, Yan W, Zhou F (2018) A novel energy dissipation outrigger system with rotational inertia damper. Advances in Structural Engineering 21(12):1865–1878. https://doi.org/10.1177/1369433218758475

Losanno D, Londono JM, Zinno S, Serino G (2018) Effective damping and frequencies of viscous damper braced structures considering the supports flexibility. Computers & Structures 207:121–131. https://doi.org/10.1016/j.compstruc.2017.07.022

Markou AA, Manolis GD (2016) Mechanical models for shear behavior in high damping rubber bearings. Soil Dynamics and Earthquake Engineering 90:221–226. https://doi.org/10.1016/j.soildyn.2016.08.035

Muscolino G, Palmeri A, Ricciardelli F (2005) Time-domain response of linear hysteretic systems to deterministic and random excitations. Earthquake Engineering & Structural Dynamics 34(9):1129–1147. https://doi.org/10.1002/eqe.471

Nagarajaiah S, Chen L, Wang M (2022) Adaptive Stiffness Structures with Dampers: Seismic and Wind Response Reduction Using Passive Negative Stiffness and Inerter Systems. Journal of Structural Engineering 148(11). https://doi.org/10.1061/(ASCE)ST.1943-541X.0003472

Nagarajaiah S, Sen D (2020) Apparent-weakening by adaptive passive stiffness shaping along the height of multistory building using negative stiffness devices and dampers for seismic protection. Engineering Structures 220:110754. https://doi.org/10.1016/j.engstruct.2020.110754

Sarlis AA, Pasala DTR, Constantinou MC, Reinhorn AM, Nagarajaiah S, Taylor DP (2013) Negative Stiffness Device for Seismic Protection of Structures. Journal of Structural Engineering 139(7):1124–1133. https://doi.org/10.1061/(ASCE)ST.1943-541X.0000616

Smith R, Merello R, Willford M (2010) Intrinsic and supplementary damping in tall buildings. Proceedings of the Institution of Civil Engineers - Structures and Buildings 163(2):111–118. https://doi.org/10.1680/stbu.2010.163.2.111

Smith RJ, Willford MR (2007) The damped outrigger concept for tall buildings. The Structural Design of Tall and Special Buildings 16(4):501–517. https://doi.org/10.1002/tal.413

Su N, Peng S, Hong N, Xia Y (2022) Wind-induced vibration absorption using inerter-based double tuned mass dampers on slender structures. Journal of Building Engineering 58:104993. https://doi.org/10.1016/j.jobe.2022.104993

Sun F-F, Wang M, Nagarajaiah S (2021) Multi-objective optimal design and seismic performance of negative stiffness damped outrigger structures considering damping cost. Engineering Structures 229:111615. https://doi.org/10.1016/j.engstruct.2020.111615

Sun T, Lai Z, Nagarajaiah S, Li H-N (2017) Negative stiffness device for seismic protection of smart base isolated benchmark building. Structural Control and Health Monitoring 24(11):e1968. https://doi.org/10.1002/stc.1968

Tan P, Fang CJ, Chang CM, Spencer BF, Zhou FL (2015) Dynamic characteristics of novel energy dissipation systems with damped outriggers. Engineering Structures 98:128–140. https://doi.org/10.1016/j.engstruct.2015.04.033

Tigli OF (2012) Optimum vibration absorber (tuned mass damper) design for linear damped systems subjected to random loads. Journal of Sound and Vibration 331(13):3035–3049. https://doi.org/10.1016/j.jsv.2012.02.017

Tsai H-C, Lin G-C (1993) Optimum tuned-mass dampers for minimizing steady-state response of support-excited and damped systems. Earthquake Engineering & Structural Dynamics 22(11):957–973. https://doi.org/10.1002/eqe.4290221104

Vickery BJ, Isyumov N, Davenport AG (1983) The role of damping, mass and stiffness in the reduction of wind effects on structures. Journal of Wind Engineering and Industrial Aerodynamics 11(1–3):285–294. https://doi.org/10.1016/0167-6105(83)90107-1

Wang M, Du X-L, Sun F-F, Nagarajaiah S, Li Y-W (2022a) Fragility analysis and inelastic seismic performance of steel braced-core-tube frame outrigger tall buildings with passive adaptive negative stiffness damped outrigger. Journal of Building Engineering 52:104428. https://doi.org/10.1016/j.jobe.2022.104428

Wang M, Liu X-H, Liu C, Sun F-F, Koetaka Y, Nagarajaiah S, Du X-L (2026) Hierarchical Simulations and Seismic Performance Evaluation of Tall Buildings Equipped with Negative Stiffness Damped Outrigger with Damping Amplification. J Struct Eng 152(3):04025291. https://doi.org/10.1061/JSENDH.STENG-15224

Wang M, Nagarajaiah S, Sun F (2022b) A novel crosswind mitigation strategy for tall buildings using negative stiffness damped outrigger systems. Structural Control and Health Monitoring 29(9). https://doi.org/10.1002/stc.2988

685 Wang M, Nagarajaiah S, Sun F-F (2020) Dynamic Characteristics and Responses of Damped Outrigger Tall Buildings
686 Using Negative Stiffness. Journal of Structural Engineering 146(12).
687 https://doi.org/10.1061/(ASCE)ST.1943-541X.0002846

688 Wang M, Nagarajaiah S, Sun F-F (2021) Optimal design of supplemental negative stiffness damped outrigger system
689 for high-rise buildings resisting multi-hazard of winds and earthquakes. Journal of Wind Engineering and
690 Industrial Aerodynamics 218:104761. https://doi.org/10.1016/j.jweia.2021.104761

691 Wang M, Sun F, Koetaka Y, Chen L, Nagarajaiah S, Du X (2023) Frequency independent damped outrigger systems
692 for multi-mode seismic control of super tall buildings with frequency independent negative stiffness
693 enhancement. Earthquake Engineering & Structural Dynamics 52(9):2731–2754.
694 https://doi.org/10.1002/eqe.3891

695 Wang M, Sun F, Nagarajaiah S (2019) Simplified optimal design of MDOF structures with negative stiffness
696 amplifying dampers based on effective damping. The Structural Design of Tall and Special Buildings 28(15).
697 https://doi.org/10.1002/tal.1664

698 Wang M, Sun F-F, Nagarajaiah S, Li Y-W (2022c) Frequency-dependency/independency analysis of damping
699 magnification effect provided by tuned inerter absorber and negative stiffness amplifying damper considering
700 soil-structure interaction. Mechanical Systems and Signal Processing 172:108965.
701 https://doi.org/10.1016/j.ymssp.2022.108965

702 Wang Y, Wang P, Qiao X, Meng H, Chen L-Q (2024) An inerter-based X-structure vibration isolator. Acta Mech
703 235(5):2539–2573. https://doi.org/10.1007/s00707-023-03846-2

704 Zhou K, Zhang J-W, Li Q-S (2022) Control performance of active tuned mass damper for mitigating wind-induced
705 vibrations of a 600-m-tall skyscraper. Journal of Building Engineering 45:103646.
706 https://doi.org/10.1016/j.jobe.2021.103646

707 **Appendix A: Mass, stiffness, and damping matrices**

708

709 The tall structure is simplified as a uniform column as a central core tube, and the Euler Bernoulli beam is adopted in
710 the present study. Each element of the beam and column is expressed as element mass, and the element mass matrix
711 is expressed as

$$M_e = \frac{mL}{420}\begin{bmatrix} 156 & 22L & 54 & -13L \\ 22L & 4L^2 & 13L & -3L^2 \\ 54 & 13L & 156 & -22L \\ -13L & -3L^2 & -22L & 4L^2 \end{bmatrix} \tag{A1}$$

$$K_e = \frac{EI}{L^3}\begin{bmatrix} 12 & 6L & -12 & 6L \\ 6L & 4L^2 & -6L & 2L^2 \\ -12 & -6L & 12 & -6L \\ 6L & 2L^2 & 6L & 4L^2 \end{bmatrix} \tag{A2}$$

712 where distributed mass along height is m; element length is L. The Rayleigh assumption obtains the damping matrix
713 C.

714 The dynamic equation of motion of a tall structure with a tuned inerter damped outrigger system is expressed as

$$M\ddot{X} + C\dot{X} + KX + \psi M_O = \Lambda F_{CW} \tag{A3}$$

715 where X is the displacement vector; the outrigger position is ψ; crosswind vector is represented as F_{CW}; the load vector
716 matrix is represented as Λ , and the resisting moment of the outrigger is represented as M_O.

The governing equations of motion of tall structure with the supplementary damper of TIDO are expressed as

$$\overline{M}\ddot{X}_s + \overline{C}\dot{X}_s + \overline{K}X_s = \overline{F}_{CW} \tag{A4}$$

where $\overline{M} = \begin{pmatrix} M & 0 \\ 0 & 0 \end{pmatrix}, \overline{C} = \begin{pmatrix} C & 0 \\ -A_2 & A_1 \end{pmatrix}, \overline{K} = \begin{pmatrix} K & \psi \\ -A_3 & 1 \end{pmatrix}, \overline{F}_{CW} = \begin{pmatrix} \Lambda F_{CW} \\ 0 \end{pmatrix} \& X_S = \begin{pmatrix} X \\ M_O \end{pmatrix}.$

Appendix B: Frequency Parameters

The frequency equations of present study are

$$4[cos(\lambda)\, cosh(\lambda) + 1] + 2C_1\lambda\Theta_1 + 2C_2\lambda\Theta_2 + C_1C_2\lambda^2\Xi_{12} = 0 \tag{B1}$$

$$\Theta_j = \begin{matrix} cos(\lambda)\, sinh(\lambda) + cosh(\lambda)\, sin(\lambda) + cos\left(\lambda(2\alpha_j - 1)\right) sinh(\lambda) \\ + cosh\left(\lambda(2\alpha_j - 1)\right) sin(\lambda) + 2\, sin\left(\lambda(2\alpha_j - 1)\right) cosh\left(\lambda(2\alpha_j - 1)\right) \\ +2\, sinh\left(\lambda(2\alpha_j - 1)\right) cos\left(\lambda(2\alpha_j - 1)\right) + 2\, cos(\alpha_j\lambda)\, sinh(\alpha_j\lambda) \\ +2\, cosh(\alpha_j\lambda)\, sin(\alpha_j\lambda), j = 1,2 \end{matrix} \tag{B2}$$

$$\Xi_{12} = \begin{matrix} 2\, sin(\lambda)\, sinh(\lambda) + 4\, sin(\alpha_2\lambda)\, sinh(\alpha_2\lambda) \\ -4\, sin(\lambda(\alpha_1 - 1))\, sinh(\lambda(\alpha_1 - 1)) \\ + sin(\lambda(2\alpha_2 - 1))\, sinh(\lambda) + sinh(\lambda(2\alpha_2 - 1))\, sin(\lambda) \\ - sinh(\lambda(2\alpha_1 - 1))\, sin(\lambda) - sin(\lambda(2\alpha_1 - 1))\, sinh(\lambda) \\ +2\, sin(\lambda(\alpha_1 + \alpha_2 - 1))\, sinh(\lambda(\alpha_1 + \alpha_2 - 1)) \\ -2\, sin(\lambda(\alpha_1 - \alpha_2 + 1))\, sinh(\lambda(\alpha_1 - \alpha_2 + 1)) \\ +2\, cosh(\lambda(\alpha_1 + \alpha_2 - 1))\, cos(\lambda(\alpha_1 - \alpha_2 + 1)) \\ -2\, cos(\lambda(\alpha_1 + \alpha_2 - 1))\, cosh(\lambda(\alpha_1 - \alpha_2 + 1)) \\ - cos(\lambda(\alpha_1 - 2\alpha_2 + 1))\, cosh(\lambda(\alpha_1 - 1)) \\ +2\, cosh(\lambda(\alpha_1 - 2\alpha_2 + 1))\, cos(\lambda(\alpha_1 - 1)) \\ -2\, sin(\lambda(\alpha_1 - 1))\, sinh(\lambda(\alpha_1 - 2\alpha_2 + 1)) \\ -2\, sinh(\lambda(\alpha_1 - 1))\, sin(\lambda(\alpha_1 - 2\alpha_2 + 1)) \\ 2\, cos(\lambda(2\alpha_1 - \alpha_2))\, cosh(\alpha_2\lambda) - 2\, cosh(\lambda(2\alpha_1 - \alpha_2))\, cos(\alpha_2\lambda) \\ -2\, sin(\lambda(2\alpha_1 - \alpha_2))\, sinh(\alpha_2\lambda) - 2\, sinh(\lambda(2\alpha_1 - \alpha_2))\, sin(\alpha_2\lambda) \\ - sin(\lambda(2\alpha_1 - 1))\, sinh(\lambda(2\alpha_2 - 1)) \\ - sin(\lambda(2\alpha_2 - 1))\, sinh(\lambda(2\alpha_1 - 1)) \\ + cos(\lambda((2\alpha_1 - 2\alpha_2 + 1))\, cosh(\lambda) - cosh(\lambda(2\alpha_1 - \alpha_2)))\, cos(\alpha_2\lambda) \\ + cos(\lambda((2\alpha_1 - 1))\, cosh(\lambda) - cosh(\lambda(2\alpha_2 - 1)))\, cos(\lambda) \\ + cos(\lambda((2\alpha_2 - 1))\, cosh(\lambda) - cosh(\lambda(2\alpha_1 - 1)))\, cos(\lambda) \\ -8\, sin(\lambda(\alpha_1 - \alpha_2))\, sinh(\lambda(\alpha_1 - \alpha_2)) \end{matrix} \tag{B3}$$

Appendix C: Stiffness expressions for higher order mode

The equivalent stiffness of the FI-TIDO system considering higher-order modes is expressed as

$$k_\theta = 2k_c r^2 \frac{s^2 C_v + k_{TIDO}}{k_c + s^2 C_v + k_{TIDO}} \tag{C1}$$

Where $s = i\omega$

$$k_\theta = \frac{EI}{\alpha H \beta} \frac{4\lambda^4 c\alpha\beta i + \eta^2}{1 + 4\lambda^4 c\alpha\beta^2 i + \eta^2} \quad \text{(C2)}$$

Where stiffness ratio between central core to perimeter columns is expressed as $\beta = \frac{EI}{2E_c A_c r^4}$, normalized outrigger damping is expressed as $c = \frac{c_v r^4}{H\sqrt{mEI}}$

Appendix D: Stability analysis

The characteristic transcendental equation for the FI-TIDO system is expressed as

$$f_1(\lambda) + f_2(\lambda) = 0 \quad \text{(D1)}$$

Where $f_1(\lambda) = k_s \begin{bmatrix} \cos(\lambda - 4\lambda\alpha)\sinh(\lambda) + \cosh(\lambda - 4\lambda\alpha)\sinh(\lambda) + 2\sinh(\lambda\alpha)\cos(\lambda\alpha) \\ +\sin(\lambda)\cosh(\lambda) + \sinh(\lambda)\cos(\lambda) - 4\cos(\lambda - 4\lambda\alpha)\sinh(\lambda - \lambda\alpha) \end{bmatrix}$ (D2)

$$f_2(\lambda) = 6\left[\cos(\lambda)\cosh(\lambda) + 2\right] \quad \text{(D3)}$$

The tall structure with FI-TIDO considering the positive solution of λ in Eq. (D1).

734 **Appendix E: Flow chart of working principle of proposed technique**

